Materials Today Chemistry 30 (2023) 101586

Contents lists available at ScienceDirect

Materials Today Chemistry

journal homepage: www.journals.elsevier.com/materials-today-chemistry/

Vaterite-nanosilver hybrids with antibacterial properties and pH-triggered release

Ana M. Ferreira [a], A. Vikulina [b], G.W.V. Cave [a], M. Loughlin [a], V. Puddu [a], D. Volodkin [a, *]

[a] School of Science and Technology, Department of Chemistry and Forensics, Nottingham Trent University, Clifton Lane, Nottingham NG11 8NS, UK
[b] Bavarian Polymer Institute, Friedrich-Alexander-Universität Erlangen-Nürnberg (FAU), Dr.-Mack-Straße, 77, Fürth 90762, Germany

ARTICLE INFO

Article history:
Received 14 October 2022
Received in revised form
2 May 2023
Accepted 3 May 2023
Available online xxx

Keywords:
Calcium carbonate
Sodium poly(4-styrenesulfonic acid) sodium salt
Recrystallization
Controlled release

ABSTRACT

Silver nanoparticles (AgNPs) have been used for over a century in various applications due to their distinctive properties. Nonetheless, the poor stability of AgNPs and adverse effects on living organisms have driven the search for materials able to protect and better control their release. Vaterite $CaCO_3$ crystals have been studied in the last two decades as carriers for different drugs due to their biocompatibility, easy synthesis and pH-sensitive properties. Herein, AgNPs were loaded into vaterite to protect, store, and control their release, resulting in $CaCO_3$/AgNPs hybrids. To tune the release of the AgNPs, the recrystallization of the hybrids into thermodynamically more stable calcite was studied and modulated with carboxymethyl−dextran (Dex^{CM}) and poly(4-styrenesulfonic acid) sodium salt (PSS), with the last one being able to stabilise the hybrids and prevent a premature release of the AgNPs at low contents (2%, w/w). The release of AgNPs from the hybrids was studied at pH 5 to 9, showing a pH-dependent release suppression for PSS-stabilised hybrids. Various mathematical models were applied to clarify the release mechanism, confirming the role of PSS in stabilising and targeting the release of AgNPs. The antibacterial studies demonstrated that the hybrids protect the AgNPs without affecting their activity, with the released nanoparticles being effective against *Escherichia coli*, methicillin-resistant *Staphylococcus aureus* and *Pseudomonas aeruginosa*. Overall, this work sheds light on the release mechanisms of AgNPs from the inorganic hybrids helping to foresee the release profiles of other compounds from vaterite.

1. Introduction

The target and controlled delivery of antimicrobial agents have been the focus of numerous works and carry on being a crucial research area due to the alarming levels of bacterial resistance [1]. Silver nanoparticles (AgNPs) are among the most used antimicrobial agents for coatings due to their good activity against a wide range of microorganisms [2]. Nonetheless, AgNPs can easily lose their colloidal stability and form aggregates with less attractive properties. Moreover, concerns have been raised in the last decades about the release of AgNPs in the environment and adverse effect on livings organisms [3]. Therefore, different works have focused on improving AgNPs stability and controlling their release through immobilization on platforms capable of protecting, storing, and releasing AgNPs [4–8].

The use of vectors/carriers to store and protect active compounds, as well as to control and target their release, opens the possibility to enhance the cargo activity and consequently improve the therapeutical effect of the encapsulated component (cargo). When it comes to nanoparticles, the use of carriers is even more crucial, as they can help to solve two major problems in nanomedicine: the low efficacy on nanoparticles delivery and potential toxicity [9].Calcium carbonate ($CaCO_3$) can be found as three different anhydrous polymorphs: aragonite, vaterite and calcite, with the first two being metastable phases that can rapidly recrystallise to calcite, the most stable phase [10]. All three polymorphs have been studied as carriers for the protection and delivery of antimicrobial, anticancer drugs, enzymes, hormones, and other biomolecules, due to their biocompatibility, availability, easy synthesis, low production costs and pH-sensitive properties [1,11–15]. In comparison with calcite and aragonite, vaterite has attracted more interest due to its porous structure, which can accommodate significant contents of different compounds [1].

Abbreviations: AgNPs, Silver nanoparticles; PVP, polyvinylpyrrolidone; Dex^{CM}, fluorescein isothiocyanate−carboxymethyl−dextran; PSS, poly(4-styrenesulfonic acid) sodium salt.

* Corresponding author.
E-mail address: dmitry.volodkin@ntu.ac.uk (D. Volodkin).

https://doi.org/10.1016/j.mtchem.2023.101586

The combination of $CaCO_3$ with AgNPs presents an opportunity to store, protect and deliver AgNPs in a controlled way, especially in acid microenvironments due the high solubility of $CaCO_3$ at low pH values. This association has been studied before to produce antimicrobial materials and surface-enhanced Raman scattering (SERS) platforms [16–22], although the mechanisms behind the release of AgNPs from $CaCO_3$ have not been extensively studied, understood and intentionally modulated.

Various works have demonstrated that the cargo release from vaterite can be triggered by the dissolution of $CaCO_3$ at acid pH or the recrystallization of vaterite into calcite [23–25]. Due to vaterite being a metastable polymorph when in solution it recrystallises into calcite. When loaded with a cargo, the transformation of vaterite (porous) into calcite (non-porous) promotes the release of the payload as it entails a dissolution/reprecipitation process and the reduction of the surface area [26]. While the recrystallization of vaterite can be used to promote a controlled and/sustained release of the cargo, when the goal is to achieve a targeted delivery at acid environments (e.g. at infection sites and tumors) the recrystallization of metastable vaterite can cause an unwanted premature delivery of the payload. Therefore, the inhibition of the recrystallization can be essential to improve the delivery at acidic sites. Previous studies have reported the partial or complete inhibition of vaterite recrystallization by adsorbing polymers on its surface through layer-by-layer (LbL) deposition, or by co-synthesis of vaterite with stabilising agents like mucin and glutamic acid [25,27–31].

A recent work published by our group has demonstrated that AgNPs can be loaded into vaterite via co-precipitation and preliminary results have demonstrated their antibacterial activity and potential for controlled release [32]. Nonetheless, questions regarding the release mechanisms of AgNPs from the hybrids, how they can be modulated, and the role of AgNPs on the antibacterial activity of the developed hybrids have not been addressed. In the present work, hybrids of $CaCO_3$ and AgNPs ($CaCO_3$/AgNPs) were produced, and their recrystallization studied. To improve the stability of the hybrids, different contents of two additives, poly(4-styrenesulfonic acid) sodium salt (PSS) and carboxymethyl–dextran (Dex^{CM}), were tested and their effect studied. The morphology, composition, and polymorphism of the $CaCO_3$/AgNPs hybrids was assessed, and the release of AgNPs was studied in a closed (no change of the buffer) and open (supernatant periodically replaced with fresh buffer solution) system, referred as closed and open-like systems, respectively. The antibacterial activity of the $CaCO_3$/AgNPs hybrids was tested against *Escherichia coli* (*E. coli*), methicillin-resistant *Staphylococcus aureus* (MRSA) and *Pseudomonas aeruginosa* (*P. aeruginosa*), three bacterial isolates responsible for numerous infections in hospital settings.

While this work is centered on AgNPs loading and release from $CaCO_3$, the findings presented here can be extrapolated to other systems and help to understand and modulate the release of different compounds of interest from vaterite.

2. Materials and methods

2.1. Materials

Sodium borohydride ($NaBH_4$, ≥99% pure), polyvinylpyrrolidone 40 kDa (PVP), fluorescein isothiocyanate–carboxymethyl–dextran 40 kDa (Dex^{CM}), poly(4-styrenesulfonic acid) sodium salt 70,000 g/mol (PSS), citric acid ($HOC(COOH)(CH_2COOH)_2$, 99.98% pure), phosphate buffered saline (PBS) tablets, Mueller Hinton broth (MHB), Mueller Hinton agar (MHA), sodium acetate ($NaCH_3COO$, ≥99% pure), TraceCERT® 10,000 ppm calcium ICP-MS standard in 5% nitric acid and TraceCERT® 1 ppm Silver ICP-MS standard in 2% nitric acid, were obtained from Sigma-Aldrich (Steinheim, Germany). Silver nitrate ($AgNO_3$, ≥99% pure), calcium chloride dihydrate ($CaCl_2.2H_2O$, ≥99% pure), sodium carbonate (Na_2CO_3, ≥99.5%), tris buffer saline 10X solution (TBS), crystal violet ($C_{25}H_{30}N_3Cl$, pure), 99% ethanol, sodium hydroxide pellets (NaOH, ≥98% pure), glacial acetic acid (CH_3COOH, ≥99.7% pure), 70% nitric acid (HNO_3, analytical grade) and 37% hydrochloric acid (HCl, analytical grade) were obtained from Fisher Scientific (Loughborough, United Kingdom).

2.2. Methods

2.2.1. Synthesis of AgNPs

AgNPs were synthesised via a chemical reduction method adapted from Nau E. et al. [33] with some modifications. Briefly, 40 ml of freshly prepared $NaBH_4$ (0.01 M) in ultrapure water was added dropwise (≈1 drop/sec) at room temperature and under constant stirring (850 rpm) to 2 ml of $AgNO_3$ (0.1 M) previously mixed with 158 ml of ultrapure water and PVP. Silver/PVP ratio (w/w) was 0.3. After the synthesis, AgNPs were filtered and then washed with deionised water by centrifugation (5000 *g* for 30 min) using Pierce™ Protein Concentrators PES with a 50 K molecular weight cut-off membrane (Thermo Fisher Scientific, Germering, Germany). The particles were then resuspended in deionised water, and the silver concentration was determined by inductively coupled plasma mass spectroscopy (ICP-MS).

2.2.2. Synthesis of bare vaterite $CaCO_3$ crystals

Bare vaterite $CaCO_3$ was synthesised based on the work of Volodkin, D. et al. [34]. Briefly, $CaCl_2.2H_2O$ (150 mM) was mixed with an equal volume of TBS 6x and ultrapure water under intense magnetic stirring (400, 650, 800 and 1400 rpm). Then Na_2CO_3 (50 mM) was added, and the stirring continued for 30 s. The suspension was poured into a tube and left for 10 min to allow the growth of the crystals. After that, the suspension was centrifuged at 3000 *g* for 5 min, washed with 25 mL of ultrapure water via resuspension, centrifuged for another 5 min, and resuspended in 300 μl of 99% ethanol. The crystals were then dried at 80 °C for 40 min. The initial molar ratio between $CaCl_2.2H_2O$ and Na_2CO_3 was 1:1. All the syntheses were performed at room temperature, and the reagents solutions were filtered with a 0.2 μm syringe-tip filter (Fisherbrand™, Loughborough, United Kingdom). Three independent syntheses were carried out per stirring speed. Transmittance images of the particles were taken under the microscope (Life Technologies EVOS FL, Invitrogen, USA) and at least 300 particles were analysed to estimate the particle size and distribution using the ImageJ software (NIH, USA).

2.2.3. Synthesis of $CaCO_3$/AgNPs hybrids

AgNPs were loaded into $CaCO_3$ crystals by co-synthesis. Briefly, $CaCl_2.2H_2O$ (150 mM) was mixed with an equal volume of TBS 6x, and then AgNPs and ultrapure water were added under different magnetic stirring speeds (400, 650, 800, or1400 rpm). A few seconds later, Na_2CO_3 (50 mM) was added, and the stirring continued for 30 s (the final volume was the same for all the syntheses). Then the suspension was poured into a tube and left for 10 min to allow the growth of the crystals. After that, the suspension was centrifuged at 3000 *g* for 5 min, washed with 25 mL of ultrapure water via resuspension, centrifuged for another 5 min, and resuspended in 300 μl of 99% ethanol. The crystals were then dried at 80 °C for 40 min. The molar ratio between $CaCl_2.2H_2O$ and Na_2CO_3 was kept the same in all the syntheses (1:1), as well as the mass ratio between AgNPs and $CaCO_3$ (30 mg/g). All the syntheses were performed at room temperature, and the reagents solutions were filtered with a 0.2 μm syringe-tip filter (Fisherbrand™,

Loughborough, United Kingdom). A minimum of 300 particles were analysed to estimate the particle size and distribution using the ImageJ software (NIH, USA). The mass of silver loaded into $CaCO_3$/AgNPs hybrids (mg/g) was determined by ICP-MS, and the loading efficiency (LE, %) and yield (%) were calculated with the following equations:

$$LE\ (\%) = \frac{m_1}{m_2} \times 100$$

where m_1 is the loaded mass of silver (mg) per gram of $CaCO_3$/AgNPs, and m_2 the total theoretical mass of silver (mg) per gram of $CaCO_3$/AgNPs hybrids.

$$Yield\ (\%) = \frac{m_3}{m_4} \times 100$$

where m_3 is the actual mass of hybrids (mg) produced per synthesis and m_4 the theoretical mass of hybrids (mg) obtained per synthesis.

2.2.4. Recrystallization studies of bare vaterite and $CaCO_3$/AgNPs hybrids into calcite

The recrystallization of bare $CaCO_3$ and $CaCO_3$/AgNPs vaterite crystals into calcite was studied to better understand the stability and release profile of the hybrids in a closed and open system. At closed-like conditions, bare $CaCO_3$ vaterite and $CaCO_3$/AgNPs hybrids were dispersed in TBS at pH 7.4 and 9.0 to a final concentration of 2 mg/ml. The samples were then incubated at 37 °C under constant agitation (500 rpm), and aliquots corresponding to 0.5% of the final volume were taken at different time points for analysis under the microscope. In the open-like system, $CaCO_3$/AgNPs hybrids were dispersed in TBS at pH 7.4 and 9.0 to a final concentration of 1.5 mg/ml and then incubated at 37 °C under constant agitation (500 rpm). At different time points, the samples were analysed under the microscope, and 75% of the supernatant was replaced with fresh buffer after centrifugation at 2000*g* for 5 min. The recrystallization of the $CaCO_3$/AgNPs hybrids with a concentration equal to 1.5 mg/ml was also studied at closed-like conditions and pH 9.0 for comparison with the results obtained at open-like conditions. In all the studies, the crystals were considered fully recrystallised when no more vaterite/spherical particles were visible (and Fig. S7). The experiment was carried in triplicate.

2.2.5. Co-synthesis of $CaCO_3$/AgNPs with Dex^{CM} and PSS, and recrystallization study

$CaCO_3$/AgNPs were co-synthesised with different contents of Dex^{CM} (1, 2, 3, 4 and 9%, initial $m_{DexCM}/m_{hybrids}$ ratio) and PSS (1, 2, 3 and 9%, initial $m_{PSS}/m_{hybrids}$ ratio) to promote $CaCO_3$ vaterite stability and prevent its recrystallization into calcite. The hybrids were co-precipitated as described in Section 2.2.3 under constant stirring (1400 rpm), with one exception, PSS or Dex^{CM} solutions (2 mg/ml) were added to the mixture just before adding Na_2CO_3. The final volume was the same for all the syntheses. To monitor the recrystallization, the hybrids were washed with ultrapure water and resuspended in TBS to a final concentration of approximately 3 mg/ml. The suspensions were then kept at 37 °C under constant agitation (500 rpm), and aliquots corresponding to 0.5% of the total volume were taken at different time points for analyses under the microscope. All the synthesises were performed at room temperature, and the reagents solutions were filtered with a 0.2 μm syringe-tip filter (Fisherbrand™, Loughborough, United Kingdom).

2.2.6. Characterization of the AgNPs, bare $CaCO_3$, $CaCO_3$/AgNPs and $CaCO_3$-PSS/AgNPs hybrids

2.2.6.1. Ultraviolet–visible (UV–Vis) spectroscopy. AgNPs present size-dependent optical properties, making UV–Vis analysis a simple and highly sensitive method to evaluate AgNPs formation, size, and stability [35,36]. Briefly, AgNPs were diluted with ultrapure water, and the UV–Vis extinction spectra were recorded in a NanoDrop One spectrophotometer (Thermo Scientific, USA) between 190 and 850 nm. The AgNPs loaded into 7-month-old hybrids were analysed after dissolving $CaCO_3$ with citric acid (1 mg/ml).

2.2.6.2. Transmission electron microscopy (TEM). AgNPs stock colloidal dispersions were diluted with ultrapure water, and 7 μl were poured on a holey carbon film copper grid (Agar Scientific Ltd, UK) and left drying overnight before analysis on a JEM-2100 Plus transmission electron microscope (Jeol, Japan) using an operating voltage of 200 kV. Around 100 particles were analysed to estimate the particle size and distribution using the ImageJ software (NIH, USA). To analyse the distribution of AgNPs into $CaCO_3$/AgNPs hybrids, the crystals were embedded in an LR White Resin (Agar Scientific Ltd, Stansted, UK) and cured for three days at 50 °C. The sample was then cross-sectioned using an Ultracut E ultramicrotome (Reichert-Jung, Wetzlar, Germany) and mounted on holey carbon film copper grids (Agar Scientific Ltd, Stansted, UK). TBS, pH 9.0, was used during the cross-sectioning step to slow down the recrystallization of the crystals from vaterite into calcite.

2.2.6.3. Induced couple plasma mass spectroscopy (ICP-MS). AgNPs colloidal dispersions, $CaCO_3$/AgNPs and $CaCO_3$-PSS/AgNPs hybrids were digested with a fresh mixture of one part of 70% HNO_3 and three parts of 37% HCl (v/v) to ensure the formation of soluble silver chloride complexes ($AgCl_x^{1-x}$) instead of insoluble AgCl salts. All the digested samples presented a concentration of silver lower than 10 μg/ml and an HCl content higher than 10% (v/v). The samples were digested at room temperature in the dark for over 1 h and then 7–14 μl of the digested samples were diluted with 1 ml of 2% HNO_3 before analysis. A calibration curve was obtained for each independent ICP analysis with silver and calcium concentrations ranging between 3 μg/L to 800 μg/L and 7 μg/L to 800 μg/L, respectively. The coefficient of determination of the standards calibration curve was always superior to 0.9984.

2.2.6.4. Scanning electron microscopy (SEM). The morphology of bare $CaCO_3$, CaCO3/AgNPs and $CaCO_3$-PSS/AgNPs hybrids was analysed by SEM (JEOL, JSM-7100f, Tokyo, Japan). The samples were mounted on stubs using double-sided carbon tape and then coated with a 5 nm thick layer of gold using a rotary pumped coater (Quorum Q150R ES, UK). Samples were analysed with a secondary electron detector and an acceleration voltage of 5.0 kV. The surface roughness was analysed using the surface plot analysis option on ImageJ software (NIH, USA). Around 100 nanocrystallites on the surface of each type of $CaCO_3$ crystal were measured using the ImageJ software (NIH, USA) to estimate the average size.

2.2.6.5. SEM coupled with energy dispersive X-ray spectroscopy (SEM-EDS). SEM-EDS was used to determine the hybrids composition and AgNPs distribution. Briefly, samples were mounted on stubs using double-sided carbon tape and then coated with a 5 nm thick layer of gold using a rotary pumped coater (Quorum Q150R ES, UK). An accelerating voltage of 10 kV and a working distance of 10 mm was used. The probe current was optimised to give a dead time around 45%.

2.2.6.6. Fourier transform infrared (FTIR) spectroscopy. The crystalline structure of bare $CaCO_3$, $CaCO_3$/AgNPs and $CaCO_3$-PSS/AgNPs microparticles were analysed by FTIR spectroscopy (Spectrum Two FTIR spectrometer, PerkinElmer, Uberlingen, Germany). For each sample, 32 scans were run between 500 and 4000 cm with a resolution of 4 cm. The ATR (attenuated total reflectance) technique was used in all the measurements. To compare different samples, the intensities of the obtained spectra were divided by the intensity of the typical band with maximum intensity at 1400-1396 cm^{-1} assigned to CO_3^{2-} anti-symmetrical stretching. AgNPs incubated in MHB were also analysed by FTIR to detect the formation of the corona composed of biomolecules. For the corona formation, AgNPs were incubated at 37 °C under constant stirring (500 rpm) in MHB (final concentration 0.38 mg/ml) for 2 h, and then the non-adsorbed biomolecules were removed by washing the AgNPs three times with ultrapure water by centrifugation (14,470 *g*, 4 °C for 30 min) and resuspension.

2.2.6.7. X-ray diffraction (XRD). The crystalline structures of bare $CaCO_3$, $CaCO_3$/AgNPs and $CaCO_3$-PSS/AgNPs microparticles were analysed on a SmartLab SE X-Ray diffractometer from Rigaku Co. Ltd. (Tokyo, Japan) with a cuppoer Kβ filter (λ = 0.1392 nm). Three independent samples per condition were scanned with a θ/2θ scan axis. The scan range varied between 20° and 80°, and the mode and speed were 1D and 5°/min, respectively. The molar percentage of vaterite and calcite was calculated based on the work of Vagena N. et al. [37]. The percentage of aragonite was assumed to be zero, and the equations below were used to determine the polymorphs molar percentage:

$$\frac{I_C^{104}}{I_V^{110}} = 7.691 \times \frac{X_C}{X_V}$$

$$100 = (X_c + X_V) \times 100$$

where 7.691 is the proportionality constant for mixtures of calcite and vaterite previously determined by Vagena N. et al. [37], I_C^{104}/Iv^{110} the ratio of the intensities of calcite and vaterite diffraction planes (104) and (110), respectively, and X_C/X_V the molar fraction ratio of calcite and vaterite.

2.2.7. Release studies of AgNPs from the hybrids

The release of AgNPs from the $CaCO_3$/AgNPs and $CaCO_3$-PSS/AgNPs hybrids was assessed in a closed and open-like system at different pH values. At closed-like conditions the release was studied at pH 5.0 (acetate buffer); pH 7.4 (TBS and MHB) and pH 9.0 (TBS). Briefly, the hybrids were incubated in the respective buffer/media at 37 °C under constant stirring (500 rpm). The final concentration was 2 mg/ml. At different time points, the samples were centrifuged at 2000 *g* for 5 min, and then aliquots corresponding to 2.3% of the total volume of supernatant were taken for calcium and silver quantification by ICP-MS. The aliquots were replaced with the same volume of fresh buffer/media to maintain the same final volume. All the experiments were carried out in triplicate.

At open-like conditions, the release was studied at pH 7.4 (TBS buffer) and pH 9.0 (TBS). Briefly, the hybrids were incubated in the respective buffer at 37 °C under constant stirring (500 rpm). The final concentration was 1.5 mg/ml. At different time points, the samples were centrifuged at 2000 *g* for 5 min, and then aliquots equal to 75% of the total volume were taken for calcium and silver quantification by ICP-MS. The aliquots were replaced with the same amount of fresh buffer to maintain the final volume. All the experiments were carried out in triplicate.

2.2.8. Kinetics model-fitting of AgNPs release from the hybrids

To better understand the mechanism of AgNPs release at open-like conditions, the experimental data was fitted to the following mathematical models:

- Hixson-Crowell model [38,39]:

$$M_\infty^{1/3} - (1 - M_t)^{1/3} = kt \quad (1)$$

Where M_t and M_∞ represent the cumulative relative amount of AgNPs released at time t and infinity, respectively, and k the release rate constant;

This model describes cases where the release of the payload is driven by its dissolution. It has been developed for crystalline drugs that dissolve in an equal manner by all sides (valid for symmetrical shapes - spheres or cubes).

- Baker-Lonsdale model [38,39]:

$$\frac{3}{2}\left[1 - \left(1 - \frac{M_t}{M_\infty}\right)^{2/3}\right] - \frac{M_t}{M_\infty} = kt \quad (2)$$

This model is based on the initial approximations of the classical Higuchi model, that describes the kinetics governed by diffusion of the payload (AgNPs) from the matrix ($CaCO_3$) which does not shrink, swell, or dissolve. This model is derived for the carriers of spherical geometry.

- Hopfenberg model [38]:

$$\frac{M_t}{M_\infty} = 1 - (1 - kt)^3 \quad (3)$$

This equation describes the release driven by surface erosion for carriers with a spherical geometry.

All experimental points have been used. Parameters M_∞ and k were calculated in Excel using Solver Add-in. For M_∞, the fitted values were limited as $M_\infty \geq$ the fraction of AgNPs released at the end time point of the experiment (48 h). R-squared coefficient was calculated as

$$R^2 = 1 - \frac{\sum (y_i - f_i)^2}{\sum (y_i - y_{av})^2}$$

where y_i is the experimental value; y_{av} is the mean of the experimental data; f_i is the predicted value from the fit.

Additionally, classical zero order kinetics model has been considered [38,39]:

$$M_t = kt \quad (4)$$

In contrast to the other three models above, which are applicable for matrix carriers, the zero-order kinetics model is valid for core-shell carriers, where the payload is protected, and its release is governed by the permeability of a 'barrier' (AgNPs are surrounded by a protective shell of the $CaCO_3$). This model is largely employed to describe cases of burst release and was applied to the experimental points before the plateau. In our experiments, good fitting to this model would mean that AgNPs release is governed by $CaCO_3$ elimination.

2.2.9. Assessment of the antibacterial activity

The antibacterial activity of the AgNPs, $CaCO_3$/AgNPs hybrids and bare $CaCO_3$ was determined against *Escherichia Coli* O157:H7 (*E. coli*), methicillin-resistant *Staphylococcus Aureus* (MRSA) and *Pseudomonas Aeruginosa* PA01 (*P. aeruginosa*). The *E. coli*, MRSA and

P. aeruginosa isolates were obtained from the American Type Culture Collection (ATCC 43888), National Collection of Type Cultures (NCTC 12493) and Nottingham Trent University (NTUCC 876), respectively.

2.2.9.1. Inoculum preparation. The bacterial isolates were streaked onto MHA plates and incubated at 37 °C for 18–24 h. For each isolate, three to four isolated colonies of the same morphological appearance were transferred into a tube containing 5 ml of MHB and then incubated overnight in a shaker at 35 °C and 225 rpm. Immediately before incubation with the hybrids or bare $CaCO_3$, overnight cultures were diluted to 1×10^6 CFU/ml.

2.2.9.2. Minimum inhibitory concentration (MIC) and minimum bactericidal concentration (MBC). The MIC was determined using the broth microdilution method adapted from Wiegand I. et al. [40], with some modifications. Briefly, AgNPs, $CaCO_3$/AgNPs and bare $CaCO_3$ were serially diluted in a 96-wells microplate with MHB to a final volume per well of 50 μl. Then 50 μl of *E. coli*, MRSA or *P. aeruginosa,* previously diluted with MHB-S to 1×10^6 CFU/ml, were added to each well. The concentrations of the AgNPs ranged between 480 and 1.875 μg/ml, and the concentrations of $CaCO_3$/AgNPs and bare $CaCO_3$ ranged between 21 and 0.328 mg/ml. The final bacterial inoculum density was 5×10^5 CFU/ml. Growth and sterility controls were included in all the plates. The microplates were incubated at 37 °C for 20 h and then read visually by observing the presence or absence of turbidity. The MIC was defined as the lowest concentration that inhibited the visible growth of the bacteria in all the replicate wells. The MBC was determined after reading the MIC and consisted of plating 10 μl of the wells without visible turbidity onto MHA-S plates. The agar plates were incubated at 37 °C for 24 h, and then read visually. The lower dilution without macroscopic bacterial growth was defined as the MBC. The experiment was repeated three to six times, with three replicates per repetition. To compare the antibacterial activity of the unloaded AgNPs with the activity of the AgNPs released from the hybrids, the amount of silver released from $CaCO_3$/AgNPs hybrids was determined (Fig. S12). Briefly, $CaCO_3$/AgNPs were serially diluted with MHB on a 96-well microplate to a final volume per well of 50 μl and then 50 μl of MHB was added. The plate was incubated at 37 °C for 24 h, and after incubation, the suspensions in each well were transferred to tubes and centrifuged at 2000 g for 5 min to sediment the hybrids. The content of silver in the supernatant was quantified by ICP-MS and the morphology of the crystals was analysed under the microscope. The experiment was carried out in triplicate and included sterility controls.

2.2.9.3. Minimum inhibitory biofilm concentration (MIBC). The MIBC determination was based on the method from Ivanova A. et al. [41] with some modifications. Briefly, AgNPs and $CaCO_3$/AgNPs were serially diluted in a 96-wells microplate with MHB to a final volume per well of 50 μl. Then 50 μl of MRSA or *P. aeruginosa,* previously diluted with MHB to 1×10^6 CFU/ml, were added to each well. The concentrations of the AgNPs ranged between 480 and 1.875 μg/ml, and the concentrations of $CaCO_3$/AgNPs and bare $CaCO_3$ ranged between 21 and 0.328 mg/ml. The final bacterial inoculum density was 5×10^5 CFU/ml. The microplates were then incubated for 24 h at 37 °C under static conditions to allow the biofilm formation. After incubation, the non-adhered bacterial cells were gently washed away three times with 150 μl of sterile PBS and then the biofilms were fixated by keeping the microplates at 60 °C for 1 h. After fixation, the biofilms were stained with crystal violet (0.1% w/v) for 1 h and then the excess of crystal violet was removed by washing the wells three times with 150 μl of sterile PBS. Between washes, the microplate was stirred at 100 rpm for 5 min. After washing, the crystal violet was dissolved with acetic acid (30% v/v, 200 μl per well). 100 μl were then transferred into a 96-well microplate, and the absorbance was read at 595 nm. The experiment was repeated at least three times in triplicate and included sterility controls. Untreated biofilms were used as positive controls. Bare $CaCO_3$ was also tested in triplicate against MRSA and *P. aeruginosa* at concentrations ranging between 21 and 0.328 mg/ml. The content of silver released from the $CaCO_3$/AgNPs hybrids was quantified by ICP-MS as described above.

3. Results and discussion

3.1. Synthesis and characterization of the AgNPs

Before producing the hybrids, AgNPs were synthesised through chemical reduction of $AgNO_3$ with $NaBH_4$ and PVP was used as a capping agent to control the growth of the nanoparticles during synthesis and improve their colloidal stability after. A stable colloid was obtained, as depicted in Fig. 1A, composed of nanoparticles with an average size of 14.2 ± 3.8 nm (Fig. 1B and D). The synthesised AgNPs presented the characteristic plasmon resonance peak with maximum absorbance (λ_{max}) around 400 nm (Fig. 1 C). The inset in Fig. 1B shows the lattice fringes with d-spacing of 2.33 Å, corresponding to the (111) plane [42,43], which demonstrates the crystalline structure of the AgNPs produced.

3.2. Loading of AgNPs into $CaCO_3$ and hybrids stabilization

The immobilization of AgNPs in vectors opens new opportunities to protect, store and release AgNPs. It also presents the chance to co-immobilise silver with other active components or use the vectors as catalytic platforms *per se*. In this work, vaterite crystals were used as vectors to immobilise AgNPs due to their environmentally friendly nature and straightforward synthesis, as well as biocompatibility and easy dissolution in acid environment or with chelating agents like EDTA [1]. In the following sections, the effect of the crystals size on the amount of silver loaded into the hybrids is presented, as well as the recrystallization studies of the hybrids into calcite.

3.2.1. Effect of $CaCO_3$/AgNPs hybrids size on AgNPs uptake

The effect of the hybrids size on vaterite loading capacity was studied to improve the uptake of AgNPs. Smaller particles tend to present higher loading capacity due to the larger surface area [44,45], however this correlation is not always found. Size changes can be associated with other alterations, like different pore size distribution or different internal structure, which can alter the capacity of the crystals to adsorb and retain the payload [45,46]. In this work, the effect of the size on the loading capacity of vaterite was analysed by synthesising $CaCO_3$/AgNPs crystals with different sizes.

The size of vaterite crystals can be tuned by varying the precursor salts concentration or ratio, pH, stirring time and speed, or even by adding additives or changing the solvent. Nonetheless, some of these parameters, like pH or salts concentration, can also affect the polymorphism of the crystals. Herein, bare vaterite crystals and $CaCO_3$/AgNPs hybrids with different sizes were synthesised by varying the stirring speeds (400, 650, 800 and 1400 rpm) as it marginally affects the polymorphism of $CaCO_3$. As presented in Fig. 2A, by increasing the stirring speed from 400 to 1400 rpm it was possible to decrease the size of bare vaterite and $CaCO_3$/AgNPs hybrids by approximately 57% and 43%, respectively. These results show the particle size dependence on the stirring speed, as higher speeds promote the formation of more nuclei and

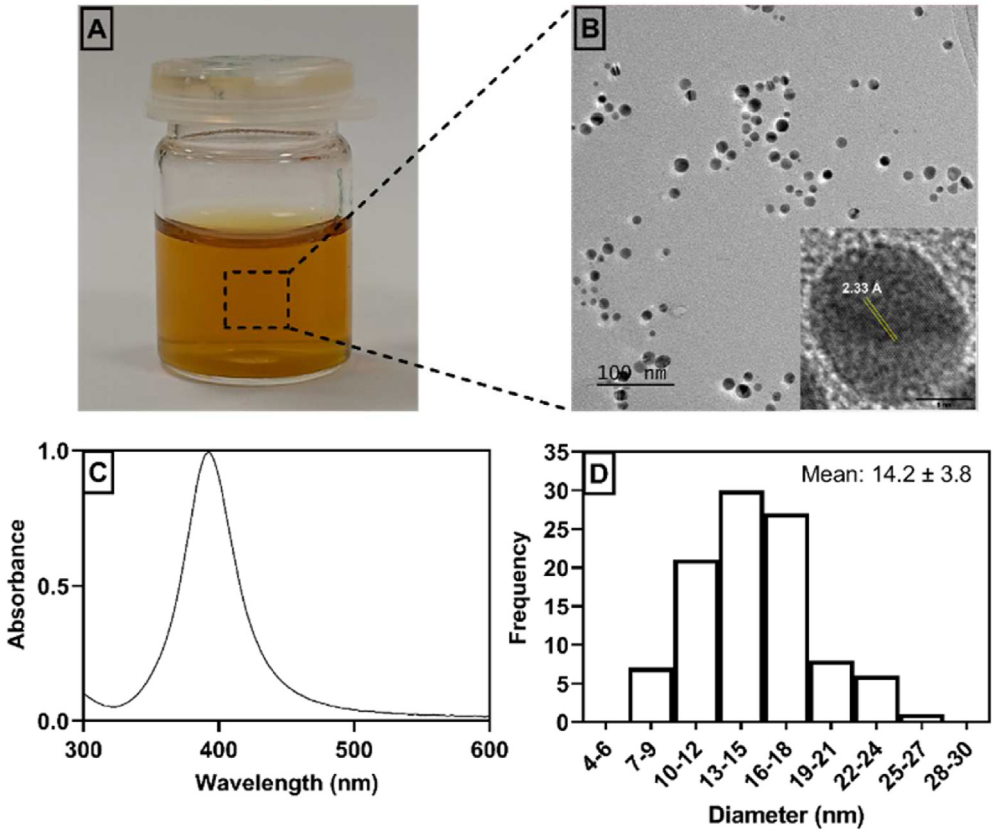

Fig. 1. Image of AgNPs colloid after synthesis (A) and respective TEM image with an inset of one nanoparticle where the lattices fringes are visible (B). The characteristic UV−Vis spectrum of the AgNPs is presented in C, and the size distribution profile and corresponding average size obtained from the analysis of the TEM images in D. The scale bar in image B corresponds to 100 nm.

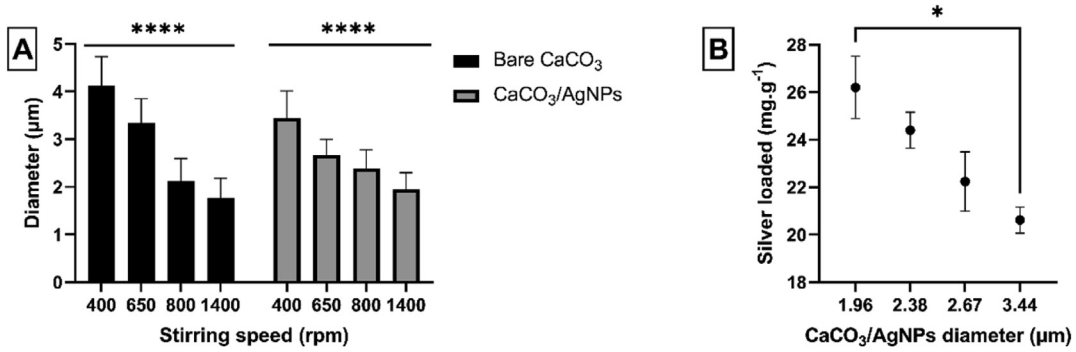

Fig. 2. Effect of the stirring speed on the size of bare $CaCO_3$ vaterite crystals and $CaCO_3$/AgNPs hybrids (A), and the size of the hybrids vs. the content of silver loaded (B). Statistical analysis made using the one-way ANOVA/Tukey's test (A) and Kruskal-Wallis/Dunn's test (B) (*$p \leq 0.05$, and ****$p \leq 0.0001$).

consequently the formation of smaller particles in this heterogeneous crystallization process [1].

Fig. 2B presents the effect of the $CaCO_3$/AgNPs hybrids size on the amount of silver loaded. The smallest crystals (2.0 ± 0.3 μm) presented a significantly higher uptake of AgNPs than the biggest ones (3.4 ± 0.6 μm), ca. 26 and 21 mg/g, respectively. Moreover, Fig. 2B depicts a clear correlation between the size and amount of AgNPs loaded, showing that when the size of the hybrids decreases, the amount of AgNPs loaded increases. These results indicate that, although not drastically, it is possible to increase the uptake of AgNPs by reducing the size of the crystals. This is associated with the smaller hybrids presenting a larger surface area, since the variation of the steering speed should only affect the initial number of nuclei formed during the start of the crystallization process [1]. Due to the higher uptake of AgNPs by the hybrids synthetised at higher stirring speeds, all the hybrids were produced at 1400 rpm.

3.2.2. *Stabilisation of $CaCO_3$/AgNPs: recrystallisation modulation*

Vaterite is a metastable polymorph of $CaCO_3$, meaning that when in solution, it tends to recrystallise into calcite, the most thermodynamically stable polymorph. When loaded, the transformation of vaterite (porous) into calcite (non-porous) promotes the release of the cargo as it entails a dissolution/reprecipitation process [26] and the reduction of the total surface area. While the recrystallization triggers and drives the release of the cargo, the affinity between $CaCO_3$ and the loaded compounds defines how

much of the payload remains free as recently demonstrated by our research group [32]. Compounds with a high affinity to $CaCO_3$ will be released and largely readsorbed into calcite, if the released content is below calcite binding capacity. On the other hand, compounds with low affinity to $CaCO_3$ will remain partly or completely free.

The recrystallization of bare $CaCO_3$ vaterite and $CaCO_3$/AgNPs hybrids was monitored over time in TBS at pH 7.4 and 9.0 as it has been demonstrated to play a crucial role in the release of AgNPs [32]. The crystals were considered fully recrystallised when there were no more spherical particles (vaterite) visible (Figs. S1 and S7). Fig. 3 presents the recrystallization time of bare $CaCO_3$ vaterite and $CaCO_3$/AgNPs hybrids into calcite at pH 7.4 and 9.0. The data shows no differences between bare $CaCO_3$ vaterite and $CaCO_3$/AgNPs hybrids, proving that AgNPs do not affect the recrystallization of vaterite. As expected, it is confirmed that the transformation of vaterite into calcite is pH-dependent, taking longer times at pH 9.0 (ca. 280 min) than at pH 7.4 (ca. 80 min). This is caused by the lower solubility of $CaCO_3$ at basic pH, which slows down the dissolution/reprecipitation process of vaterite into calcite.

While recrystallization can be used to control the release of the cargo, it does not enable a targeted release in acidic environments, like infection sites or tumors. Therefore, changing or even halting the recrystallization of vaterite into calcite is of interest, as it would allow the modulation and controlled release of the cargo. On that front, researchers have been inspired by the occurrence of vaterite in nature. Despite vaterite being a metastable polymorph, it can be found on gastropod eggshells and gallstones, either as a precursor or a structural component [47]. It is believed that such existence is possible through the stabilization of vaterite with inorganic or organic components [47]. In a biomimicry type of approach, vaterite has been stabilised by associating it with ions, macromolecules or polymers [47].

In the present work, the effect of different quantities of PSS (1–9%, initial $m_{PSS}/m_{hybrids}$ ratio) and Dex^{CM} (1–9%, initial m_{DexCM}/m_{hyrid} ratio) was tested in an attempt to develop stable hybrids.

PSS has been used by numerous researchers as an additive for the synthesis of vaterite, as it favors the growth of vaterite over calcite [48–51], while Dex^{CM} has only recently been reported as a good stabiliser for vaterite [52]. In both cases, it is believed that the stabilization of vaterite is promoted by the interactions of Ca^{2+} with the negatively charged groups present on the polymer chains [47,48], which initially work as centers of nucleation (due to the localised high concentration of Ca^{2+} around the polymers chains) and then as stabilization agents through absorption on vaterite phase [53,54].

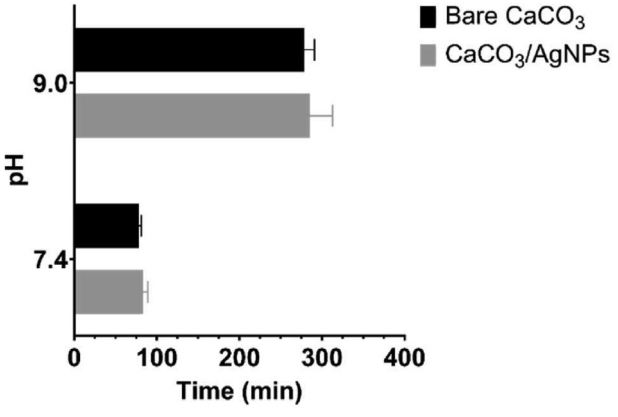

Fig. 3. Duration of the recrystallization of bare $CaCO_3$ vaterite and $CaCO_3$/AgNP hybrids into calcite in TBS at pH 7.4 and 9.0.

Table S1 summarises the effect of PSS and Dex^{CM} on the recrystallization of $CaCO_3$/AgNPs hybrids over 15 days. Overall, all the crystals synthesised with Dex^{CM} and PSS presented better stability, with the recrystallization being delayed or totally prevented for at least 15 days. Dex^{CM} at 2 and 3% prevented the hybrids from fully recrystallising within seven days, which was extended to 15 days when the crystals were synthesised with 4% of Dex^{CM}. Nonetheless, although the recrystallization was clearly delayed with 4% of Dex^{CM}, it did not halt the dissolution/reprecipitation of vaterite into calcite, proven by the presence of calcite and depleted vaterite crystals in solution after 9 and 15 days (Fig. S2).

Another intriguing effect of Dex^{CM} on the hybrids was the inhibition of AgNPs uptake by $CaCO_3$. As presented in Fig. S2, by increasing the amount of Dex^{CM} the content of AgNPs loaded into the hybrids dropped, as evidenced by the intensification of the amber color of the supernatant (more AgNPs in suspension) and whitening of the crystals. This effect might result from Dex^{CM} changing the affinity between $CaCO_3$ and AgNPs and altering the structure of the crystals and consequently decreasing the adsorption of AgNPs.

In the case of the $CaCO_3$-PSS/AgNPs hybrids, 1 and 2% of PSS added during synthesis inhibited the complete recrystallization of the hybrids within 7 and 15 days, respectively. Crystals synthesised with 2%, 3% and ~9% of PSS, did not present calcite after 15 days nor depleted vaterite crystals (Fig. S2), which indicates that the recrystallization was entirely halted. Moreover, PSS did not affect the uptake of AgNPs at the concentrations tested (Fig. S2). These results demonstrate that PSS is a better stabilising agent for the $CaCO_3$/AgNPs hybrids, which might be explained by the much higher density of anionic groups on PSS (one sulfonate group per each sodium 4-vinylbenzenesulfonate monomer) than on Dex^{CM} (ca. one O-carboxymethyl group per every five glucose monomers), which results in the growth of hybrid vaterite crystals energetically more favorable [53].

Overall, the results here presented highlight the effect of stabilising agents on the recrystallization of vaterite, and their effect on the loading of AgNPs, demonstrating that the final properties of the crystals must be considered when choosing a stabilising agent.

Due to PSS not affecting the uptake of AgNPs and halting the recrystallization of $CaCO_3$, the work was further carried on with the hybrids synthesised with 2% of PSS.

3.3. Characterization of the hybrids

3.3.1. Composition and morphology

$CaCO_3$/AgNPs hybrids, with or without PSS, were synthesised at the optimised synthesis conditions. Table 1 presents the size and content of silver loaded into $CaCO_3$/AgNPs and $CaCO_3$-PSS/AgNPs hybrids, as well as the loading efficiency and yield per synthesis. Overall, $CaCO_3$-AgNPs and $CaCO_3$-PSS/AgNPs hybrids presented similar sizes, around 2 μm, and similar silver contents, i.e. approx. 26 mg/g. This was reflected on the high loading efficiencies, 90 and 89%, also favored by the small size of the hybrids, as demonstrated in the sections above. The yield per synthesis was also similar between the hybrids, ca. 68%, with about 32% being lost due to the synthesis steps (reaction, centrifugation, washing and drying). The data in Table 1 shows that PSS did not considerably affect the size of the hybrids, content of AgNPs loaded or the yield per synthesis.

The high loading efficiencies (ca. 87%) demonstrate that the synthesis process presented here can minimise AgNPs waste, an important consideration due to the potential adverse effects of silver in the environment. Moreover, the AgNPs that were not uptaken by the hybrids can be washed and re-used as their properties are kept, as shown by the UV–Vis of the surplus AgNPs retrieved from the synthesis medium (Fig. S3).

Table 1
$CaCO_3$/AgNPs and $CaCO_3$-PSS/AgNPs hybrids size, mass of the silver (mg/g) loaded, loading efficiency and yield per synthesis.

	Diameter (μm)	Silver content (mg of silver per g of hybrids)	Loading efficiency (%)	Yield (%)
$CaCO_3$/AgNPs	1.9 ± 0.8	26.3 ± 2.4	90.4 ± 8.2	68.9 ± 2.3
$CaCO_3$-PSS/AgNPs	2.1 ± 1.0	26.0 ± 3.4	89.1 ± 11.8	68.0 ± 4.9

The stability of AgNPs over time is of significant importance as it assures that the optical and antimicrobial properties are maintained for prolonged periods. To test the suitability of the hybrids to store AgNPs, AgNPs loaded into 7-month-old hybrids were analysed by UV−Vis spectrophotometry. As shown in Fig. S4, the AgNPs stored in the hybrids for 7 months presented the same characteristic peak with maximum absorbance around 400 nm, without any major shifts, indicating that there were not significant changes in size during the storage period. This proves that the hybrids are good platforms to store AgNPs at room temperature for at least 7 months, an advantage in comparison with silver colloidal suspensions that must be stored at 4 °C to preserve the properties of the nanoparticles.

The hybrids morphology and surface characteristics were also analysed using SEM. As presented in Fig. 4, all the synthesised crystals (bare $CaCO_3$, $CaCO_3$/AgNPs, $CaCO_3$-PSS and $CaCO_3$-PSS/AgNPs) presented a spherical structure composed of small nanocrystallites, a typical feature of $CaCO_3$ vaterite. Interestingly, the crystals co-synthesised with AgNPs presented slightly smaller nanocrystallites, as evidenced in Fig. 4B, although the most significant difference was noticed between the crystals with and without PSS. The crystals co-synthesised with PSS had significantly smaller nanocrystallites (sizes between 43 and 54 nm) than those synthesised without PSS (sizes between 81 and 99 nm). This resulted in the crystals with PSS presenting smoother surfaces, as demonstrated by the surface analysis in Fig. 4C. The effect was caused by PSS controlling the nucleation process and adsorbing on the surface of the nanocrystallites preventing further growth [53,54].

3.3.2. Silver nanoparticles distribution

Previous results have demonstrated that $CaCO_3$/AgNPs hybrids present an even distribution of AgNPs [32]. To corroborate these results and study the effect of different synthesis conditions, crystals size, and the effect of PSS on the distribution of the AgNPs, SEM-EDS analysis was carried out. Fig. 5 presents the mapping images and respective spectrograms of $CaCO_3$/AgNPs and $CaCO_3$-PSS/AgNPs hybrids. As expected, the data confirmed that the hybrids are mainly composed of calcium, oxygen and carbon, although the carbon peak also resulted from the carbon tape used to mount the samples. The gold peak in the spectrogram resulted from the gold coating on the samples for SEM-EDS analysis. In the mapping images it is possible to see the uniform distribution of AgNPs on the hybrids and confirm that the AgNPs are embedded on the crystals, which is also corroborated by the characteristic peaks of silver on the spectrogram at 2.98 and 3.15 KeV. Once again, it is demonstrated that PSS did not affect the distribution of the AgNPs, although it is not possible to exclude that the nanoparticles might be localised at different depths. Moreover, in comparison with previous results published by our group for larger crystals (3−4 μm) [32], the results show that changes in the synthesis conditions and size did not affect the distribution of the AgNPs.

3.3.3. Polymorphism

The polymorphism of $CaCO_3$ is of utmost importance as it affects the surface area and the cargo release mechanism. The polymorphism of the crystals loaded with silver, and with or without PSS, was assessed through FTIR and XRD analysis. Fig. 6 presents the FTIR spectra of bare vaterite, bare calcite, $CaCO_3$/AgNPs, $CaCO_3$-PSS and $CaCO_3$-PSS/AgNPs hybrids. All the spectra presented three characteristic peaks with similar intensities with maximum transmittance at 848−850 cm^{-1}, 872−874 cm^{-1}, and 1396−1401 cm^{-1}, which correspond to CO_3^{2-} out-of-plane bending (ν_2 mode) and antisymmetrical stretching (ν_3 mode), respectively [55,56]. Shifts on these peaks were caused by the type of polymorph or polymorphs ratio in each sample, and interactions of $CaCO_3$ with other components, such as AgNPs, the corresponding capping agents and PSS [57].

The bare calcite sample presented the characteristic peaks with maximum transmittance at 712 cm^{-1} and 1795 cm^{-1}, and a single peak with maximum transmittance around 1400 cm^{-1}. These peaks correspond to CO_3^{2-} in-plane bending (ν_4 mode), $\nu_1 + \nu_4$ mode, and ν_3 mode, respectively [56,58]. Bare vaterite also presented its characteristic peaks at 745 cm^{-1} (ν_4 mode), 1088 cm^{-1} (ν_1 mode) and a split and broad band around 1400−1459 cm^{-1} (ν_3 mode) due to the asymmetry around the carbonate ion [59].

The spectra of $CaCO_3$/AgNPs and $CaCO_3$-PSS/AgNPs hybrids presented the unique peaks assigned to the vaterite phase at 745 cm^{-1} and 1088 cm^{-1}, as well as the split and broad band around 1398−1461 cm^{-1}. A peak with very low intensity was also detected at 713 cm^{-1}, which indicates the presence of small quantities of calcite in both samples. This is corroborated by the XRD data, where it is possible to detect a low-intensity peak assigned to calcite (Fig. S6).

The samples with PSS ($CaCO_3$-PSS and $CaCO_3$-PSS/AgNPs) presented four unique peaks at 1181 cm^{-1}, 1130/1131 cm^{-1}, 1045/1046 cm^{-1} and 1010 cm^{-1}, which corresponded to PSS (Fig. S5) and evidenced its incorporation into the crystals. The peaks at 1181 cm^{-1} and 1045/1046 cm^{-1} corresponded to the asymmetric and symmetric vibrations of the sulfonate group in PSS, and the peaks at 1130/1131 cm^{-1} and 1010 cm^{-1} to in-plane skeleton vibrations and in-plane bending of the benzene ring [60−62]. The band shifts were due to the interaction of $CaCO_3$ with PSS, mainly the sulfonate group, which are responsible for vaterite stability.

Table 2 presents the molar percentage (% mol) of vaterite in the samples bare $CaCO_3$, $CaCO_3$/AgNPs, $CaCO_3$-PSS and $CaCO_3$-PSS/AgNPs determined through analysis of the XRD data (Fig. S6). The results show that all the synthesised crystals present a high content of vaterite, between 86% and 94%, proving that the main phase of $CaCO_3$/AgNPs and $CaCO_3$-PSS/AgNPs hybrids is vaterite. Moreover, the data shows that AgNPs and PSS did not affect the predominant $CaCO_3$ phase, as corroborated by the SEM images (Fig. 4A) where mainly vaterite crystals are visible (spherical shape particles).

3.4. AgNPs release

Various studies have proposed that the release of the cargo from $CaCO_3$ vaterite crystals results from the recrystallization of vaterite into calcite, diffusion, or the dissolution of $CaCO_3$ at low pH values or in the presence of calcium chelating agents [1,63,64]. The predominant release mechanism is triggered and/or affected by the properties of the cargo, the cargo-vector interactions, and external conditions (composition of the media, pH, temperature, etc.) and

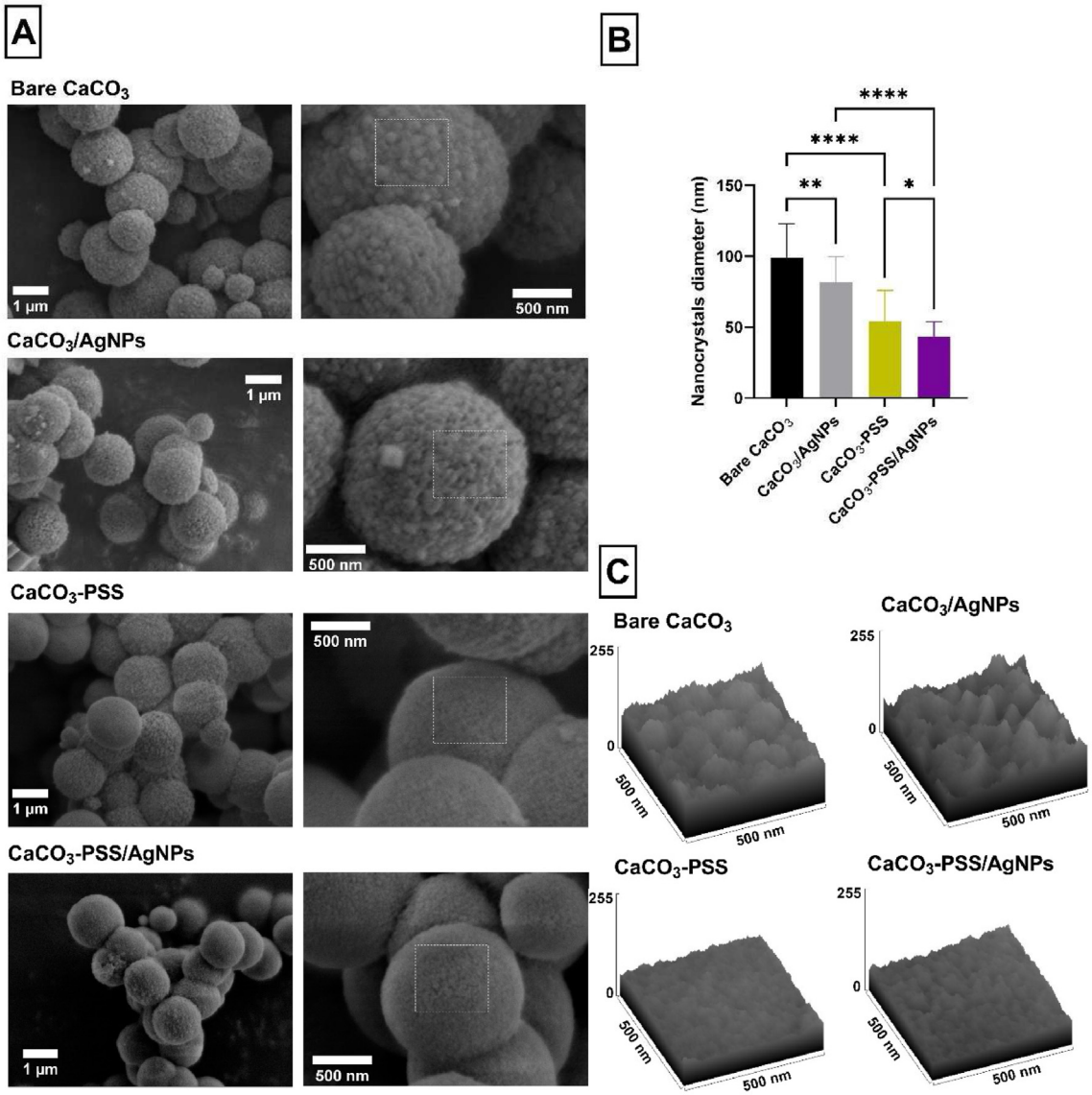

Fig. 4. SEM images of bare $CaCO_3$, $CaCO_3$/AgNPs, $CaCO_3$-PSS and $CaCO_3$-PSS/AgNPs (A) and the respective average size of the nanocrystallites (B) and surface roughness plots of the areas marked in grey outline on the SEM images (D). Statistical analysis made using the Kruskal-Wallis/Dunn's test (*$p \leq 0.05$, **$p \leq 0.01$ and ****$p \leq 0.0001$). The scale bars in image A (left) correspond to 1 μm and in image A (right) to 500 nm.

can occur concomitantly with other release mechanisms. A recent publication by our group has demonstrated that the release of AgNPs from vaterite hybrids occurs via dissolution at acidic conditions, while at neutral and basic conditions, the recrystallization of vaterite to non-porous calcite, and the affinity of AgNPs to $CaCO_3$ governs the release [32]. Despite these results and progress in understanding the release mechanisms of the payload from vaterite, there are still areas that need further clarification, like to which extent the recrystallization drives the release of the cargo and the effect of external factors, like the media composition. In the following sections, the different release mechanisms of AgNPs from the hybrids are studied in more detail, and the effect of PSS, pH value, type of release system and media is analysed.

3.4.1. Release of AgNPs in saline buffer

Figs. 7 and 8 present the release of silver and calcium ions from $CaCO_3$/AgNPs and $CaCO_3$-PSS/AgNPs hybrids, respectively, in saline buffers at different pH values. The release was assessed at closed and open-like conditions to study the main mechanisms behind AgNPs release from vaterite.

At closed-like conditions, $CaCO_3$/AgNPs presented a burst release of AgNPs at pH 5.0, which was promoted by the dissolution of the crystals, as corroborated by the high amount of calcium ions released, ca. 80% of the total calcium in the hybrids. At pH 7.4 and 9.0 there was a slower release, with the maximum amount of AgNPs being released within 2 (47 ± 1%) and 5 h (56 ± 6%), respectively. This was not accompanied by the dissolution of $CaCO_3$, and the maximum release coincided with the end of the crystals recrystallization (Fig. 3 and Fig. S1), demonstrating that the transformation of vaterite into calcite promoted the partial release of the cargo. The hybrids released more silver at pH 9.0 than at pH 7.4, due to the longer recrystallization times, which made the process more selective and therefore, lower contents of AgNPs were entrapped into calcite, as demonstrated before by our group [32]. It is noteworthy that calcite crystals can also work as carriers for AgNPs. After vaterite recrystallization, the newly formed calcite crystals

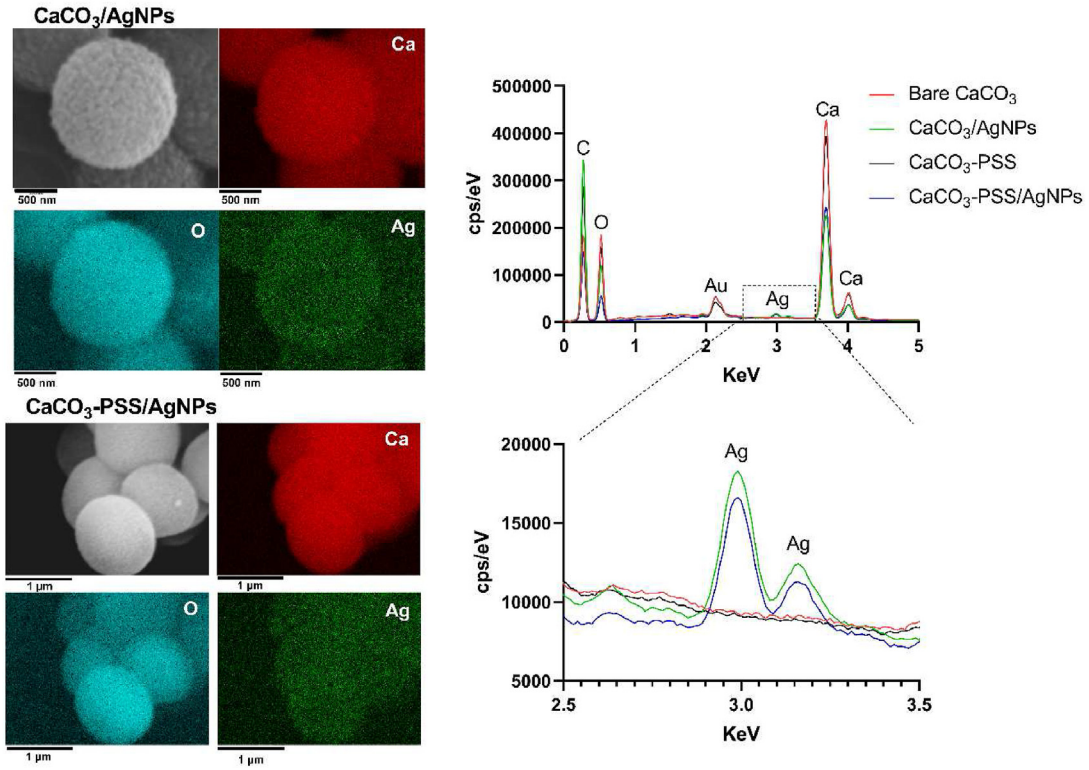

Fig. 5. SEM-EDS mapping images and respective spectrograms of $CaCO_3$/AgNPs and $CaCO_3$-PSS/AgNPs hybrids. Initial $CaCO_3$/AgNPs ratio equal to 3% (w/w). The scale bars in the $CaCO_3$/AgNPs hybrids images correspond to 500 nm and in the $CaCO_3$/PSS/AgNPs hybrids images to 1 μm.

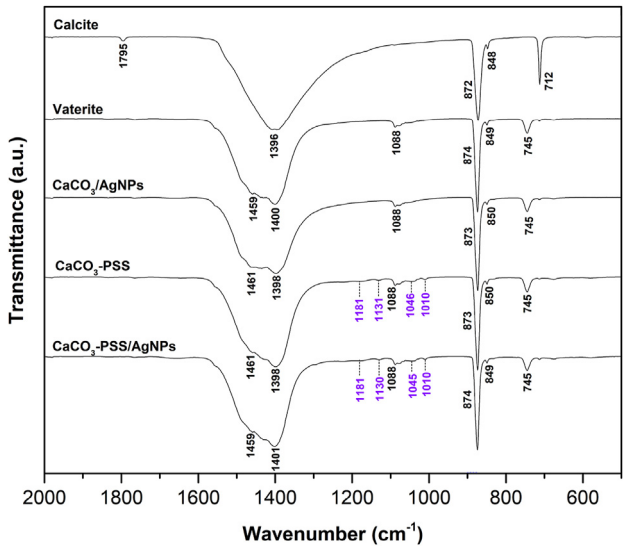

Fig. 6. FTIR spectra of bare vaterite and calcite crystals, $CaCO_3$-PSS, $CaCO_3$/AgNPs and $CaCO_3$-PSS/AgNPs hybrids. Purple wavenumbers correspond to characteristic bands of PSS.

Table 2
Vaterite molar percentage (mol%).

	Vaterite (mol%)
Vaterite/Bare $CaCO_3$	93.8 ± 2.1
$CaCO_3$/AgNPs	86.2 ± 7.5
$CaCO_3$-PSS	93.5 ± 0.2
$CaCO_3$-PSS/AgNPs	91.8 ± 1.7

retained around 53 and 44% of AgNPs at pH 7.4 and 9.0, respectively, with no further significant release of AgNPs being detected in the following hours. Therefore, it is demonstrated that the vaterite-to-calcite recrystallization promoted the partial release of the cargo, and although the recrystallization triggers the release of the payload, calcite can also uptake the cargo and prevent a complete release. The amount of the payload that remains free depends on the affinity between the cargo and $CaCO_3$ [32]. These results show that at closed-like conditions, the pH and recrystallisation are the main factors governing the release mechanism of AgNPs from $CaCO_3$.

The release of AgNPs and calcium ions at pH 7.4 and 9.0 was also studied at open-like conditions (Fig. 7B and D), where the supernatant was periodically removed and replaced with fresh buffer. This was not carried at pH 5.0, as the results from the experiment at closed conditions demonstrated that at low pH values the crystals dissolve and have an immediate burst release of AgNPs.

The data presented in Fig. 7B and D, shows that at pH 7.4 the release was mainly driven by the dissolution of the hybrids (81% of calcium released), and to a lower extent, by the transformation of vaterite into calcite, as demonstrated by the recrystallization studies at open-like conditions (Fig. S7). This resulted in approximately 74% of silver being released after 48 h. On the other hand, at pH 9.0 almost no silver was released despite the continued replacement of the buffer. This was caused by the low solubility of $CaCO_3$ at basic pH and the continuous removal of dissolved $CaCO_3$, when replacing the supernatant with fresh buffer, which delayed the recrystallization of vaterite into calcite. This was corroborated by the recrystallization studies at open-like conditions (Fig. S7), where it was demonstrated that the continuous replacement of the buffer delayed the recrystallization of vaterite into calcite. This was more drastically noticed at pH 9.0, where the hybrids recrystallization into calcite took more than 48 h (Fig. S7).

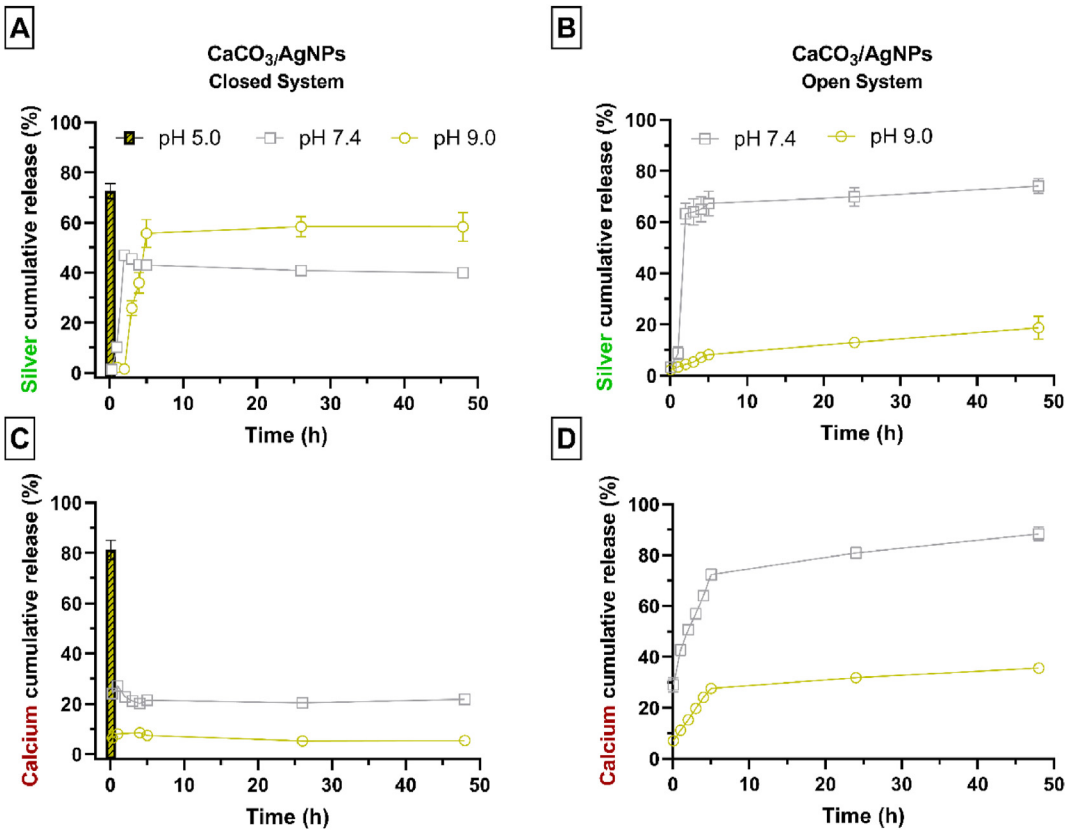

Fig. 7. Cumulative release over time of silver (A and B) and calcium ions (C and D) from $CaCO_3$/AgNPs hybrids at pH 5.0, 7.4 and 9.0 at closed (A and C) and open-like (B and D) conditions.

The effect of PSS on the release of AgNPs from the hybrids was also analysed under the same conditions. As mentioned in the previous sections, PSS is a negatively charged polymer that can stabilise vaterite crystals and prevent the recrystallization into calcite.

As shown in Fig. 8, at closed-like conditions, the hybrids synthesised with PSS did not release AgNPs at pH 7.4 and pH 9.0 as they did not recrystallise (Fig. S8). On the other hand, at pH 5.0 there was an immediate burst release, with over 90% of AgNPs being released. This was promoted by the dissolution of $CaCO_3$ at acidic pH, demonstrated by the high amount of calcium ions in the solution (ca. 90%). These results highlight the importance of recrystallization in triggering the release of AgNPs, and that by controlling it, is possible to target the cargo release at acidic conditions. This is a highly desirable property for the target release of drugs at infection and inflammation sites, as well as at the core of biofilms or tumors, where an acidic microenvironment is mostly predominant.

The release of AgNPs from $CaCO_3$-PSS/AgNPs was also studied at open-like conditions (Fig. 8B and D). At pH 9.0 there was no release of silver, once again due to the low solubility of $CaCO_3$ at basic pH. At pH 7.4 about 60% of silver was released after 6 h due to the continuous dissolution of the crystals promoted by the frequent replacement of the buffer. Interestingly, the release profile of calcium at pH 7.4 demonstrated that ca. 80% of $CaCO_3$ had to be dissolved for a significant release of silver to happen. This was lower for the hybrids synthesised without PSS, where about 40% of the crystals have to be dissolved before a significant release of AgNPs. This difference might be due to the recrystallization also playing a role in the release of silver from the $CaCO_3$/AgNPs hybrids and the lower stability of the hybrids without PSS. Nonetheless, despite these differences, the data show that the hybrids just released AgNPs when their structure was significantly affected by the dissolution of $CaCO_3$, which can be explained by the unique structure of vaterite and the good affinity between $CaCO_3$ and AgNPs.

To better understand the mechanism of AgNPs release, the experimental points obtained at open-like conditions (pH 7.4 and 9.0) were fitted to four mathematical models, which predict different mechanisms of release: dissolution of the payload (AgNPs), surface erosion of the matrix ($CaCO_3$), and diffusion of AgNPs from the hybrid crystals.

The parameters obtained through fitting the experimental data to these models are summarised in Table 3.

As expected, there was not a good fitting to the Hixon-Crowell model as AgNPs do not undergo dissolution under the release experiments conditions. At pH 7.4, the results of the fitting suggest that the release of AgNPs from $CaCO_3$/AgNPs hybrids is governed by the dissolution of $CaCO_3$, since the fitting to the zero-order kinetics describes well the experimental data (highest R^2). At pH 9.0, R^2 values are high ($\geq$0.95) and similar between two models, Baker-Lonsdale and Hopfenberg, predicting AgNPs diffusion and $CaCO_3$ erosion, respectively. It seems that both phenomena play a role in the release of AgNPs from $CaCO_3$/AgNPs hybrids at higher pH values. Although the zero-order equation also describes well the experimental data at pH 9.0, it is unlikely that it represents the mechanism of release, because the high R^2 in this case is attributed to the fact that the experimental points after 5 h of release were not included into the fitting due to the limitations associated with Equation 4. If all the data points had been included, the R^2 would drop down to 0.831 ($k = 0.0044$). This limitation is not applicable to the data at pH 7.4, because the plateau was almost completely reached within 5 h (ca. 70% of the total amount of AgNPs was released within the first 5 h).

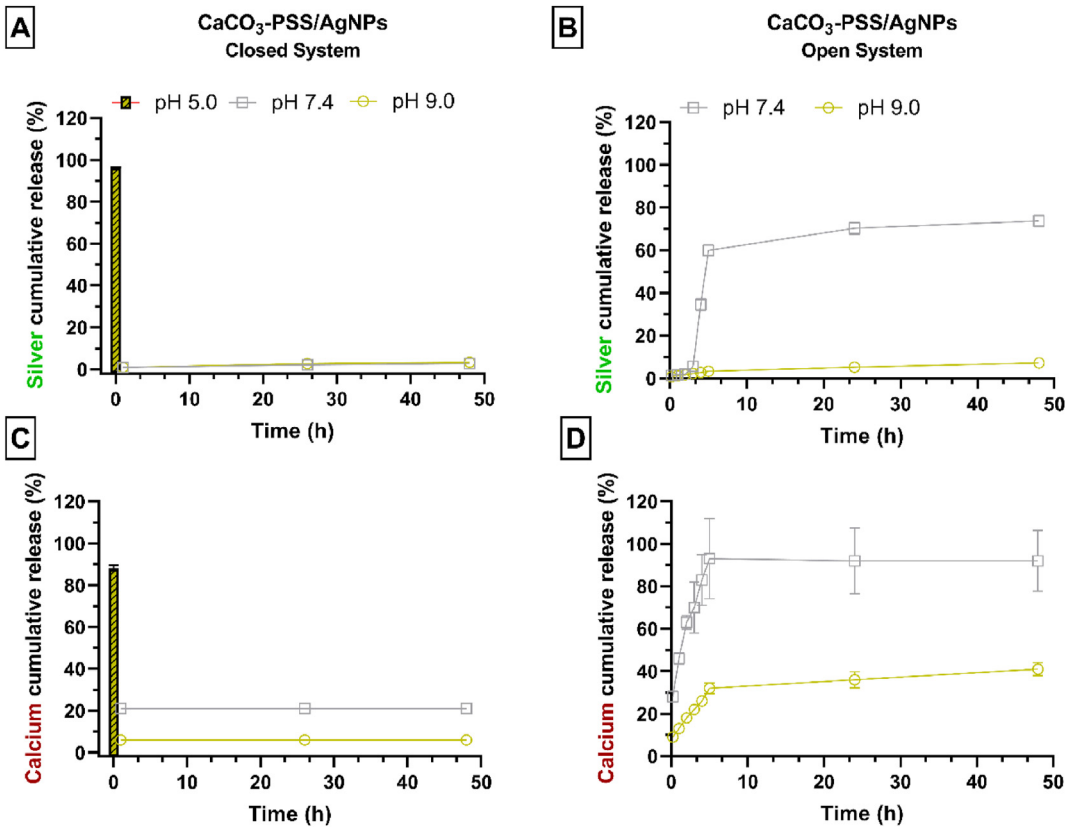

Fig. 8. Cumulative release over time of silver (A and B) and calcium (C and D) from $CaCO_3$-PSS/AgNPs hybrids at pH 5.0, 7.4 and 9.0 at closed (A and C) and open-like (B and D) conditions.

Table 3
Calculated parameters obtained by fitting of the experimental data from the release studies at open-like conditions to mathematical models that reflect different release mechanisms. M_∞ is the maximum fraction of silver released. k is the rate constant. Parameter M_∞ is not applicable for zero-order model.

Model	Mechanism	$CaCO_3$/AgNPs				$CaCO_3$-PSS/AgNPs			
		pH 7.4		pH 9.0		pH 7.4		pH 9.0	
		M_∞, k [h^{-1}]	R^2	M_∞, k [h^{-1}]	R^2	M_∞, k [h^{-1}]	R^2	M_∞, k [h^{-1}]	R^2
Hixson-Crowell	Dissolution of AgNPs	0.79, 0.015	0.286	0.96, 0.0012	0.935	0.95, 0.011	0.663	0.98, 0.0005	0.905
Baker-Lonsdale	Diffusion of AgNPs	0.74, 0.017	0.558	**0.40, 0.0010**	**0.989**	**0.73, 0.012**	**0.894**	**0.104, 0.0033**	**0.993**
Hopfenberg	Erosion of $CaCO_3$	0.74, 0.030	0.533	**0.187, 0.019**	**0.948**	0.73, 0.030	0,836	0.072, 0.020	0,953
Zero-order (until 5 h)	$CaCO_3$ shell	N/A, **0.268**	**0.892**	N/A, 0.0178	0.962	0.084	0.799	0.0071	0.973
Zero-order (all data)	elimination	N/A	N/A	N/A, 0.0044	0.831	N/A	N/A	0.174	0.823

The release of AgNPs from $CaCO_3$-PSS/AgNPs hybrids obeys the Baker-Lonsdale diffusion model, supporting the conclusion that PSS stabilises vaterite and suppresses its recrystallization. Hopfenberg model also provides satisfactorily high R^2 values, which supports the role of slow $CaCO_3$ erosion in the release mechanism. The good fit of the zero-order kinetics is attributed to the same artefact effect of the fitting as described above for $CaCO_3$/AgNPs hybrids. If all the data points from $CaCO_3$-PSS/AgNPs at pH 9.0 would be included the R^2 would drop down to 0.823 ($k = 0.174$).

The fitting of the experimental curves to the release mechanism models are shown in Fig. S9. Fig. 9 presents an outline of the main release mechanism of AgNPs in buffer saline.

3.4.2. Release of AgNPs in the presence of proteins and carbohydrates

The recrystallization of vaterite is a complex process that, as demonstrated before, can be affected by several factors. Less than twenty years ago, the 'corona effect' on nanoparticles was reported. It describes the adsorption of proteins, carbohydrates, lipids, nucleic acids, and other molecules onto the surface of nanoparticles when they are mixed with biologic fluids or media rich in biomolecules [9]. Herein, MHB, the medium used to perform the antibacterial tests, was used to study the release behavior of the hybrids when exposed to high contents of proteins and carbohydrates at pH 7.4.

As depicted in Fig. 10, 39 and 18% of silver was released from $CaCO_3$/AgNPs and $CaCO_3$-PSS/AgNPs within 1 h, and 53% and 34% after 96 h, respectively. Although it is clear that PSS retarded the release of the AgNPs, and that both types of hybrids presented a very slow release in MHB, the hybrids with PSS did not present a release profile similar to the one in saline buffer at pH 7.4, where almost all the silver remained embedded in the hybrids. Interestingly, the hybrids presented good stability in MHB, with no recrystallization detected within 96 h (Fig. S10), even for the crystals without PSS. This evidenced that recrystallization was not the driving force for the release of AgNPs.

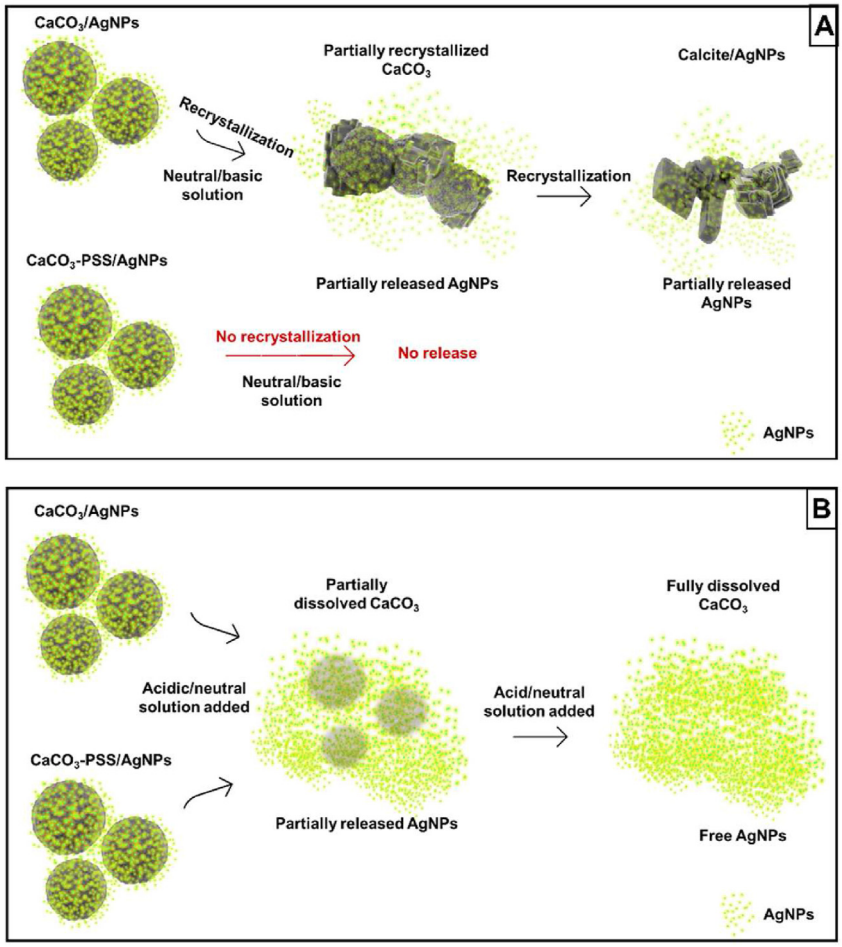

Fig. 9. AgNPs main release mechanisms in saline buffer solutions: recrystallization (A) and dissolution (B).

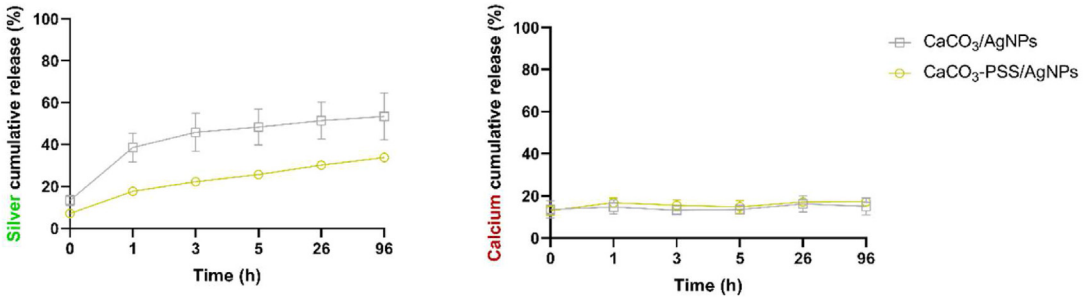

Fig. 10. Cumulative release over time of silver (left) and calcium (right) from $CaCO_3$/AgNPs and $CaCO_3$-PSS/AgNPs hybrids in MHB.

The need for the microparticles to decrease their surface energy, and the proteins and carbohydrates in the medium to minimise their free enthalpy, favored the adsorption of these biomolecules on the surface of $CaCO_3$ and AgNPs, forming a corona through electrostatic, hydrophobic and van der Waals interactions [9].

The formation of a corona on $CaCO_3$ surface has previously been reported and used to prevent or retard the recrystallization of vaterite and therefore, the cargo release [65–67]. Nonetheless, to the best of our knowledge, the opposite effect, i.e. the corona triggering the cargo release from vaterite has not been reported before. We believe, that while the biomolecules that compose the corona promote the stability of vaterite and halt the recrystallization, which is desirable, they are also adsorbed onto the surface of the AgNPs (as demonstrated by the FTIR data in Fig. S11), decreasing the affinity between the AgNPs and $CaCO_3$. Therefore, poorly entrapped AgNPs are eventually released due to the low affinity to $CaCO_3$. This is potentiated by the depletion of 13–17% of calcium from the surface of some of the hybrids, as demonstrated in Fig. 10 which facilitated the release of AgNPs. This is also corroborated by the images in Fig. 11 which present hybrids with partially depleted surfaces.

Although the release of AgNPs was more accentuated in the first hour, it slowly carried on throughout the incubation period. This might be due to the corona formation steps, which entail the

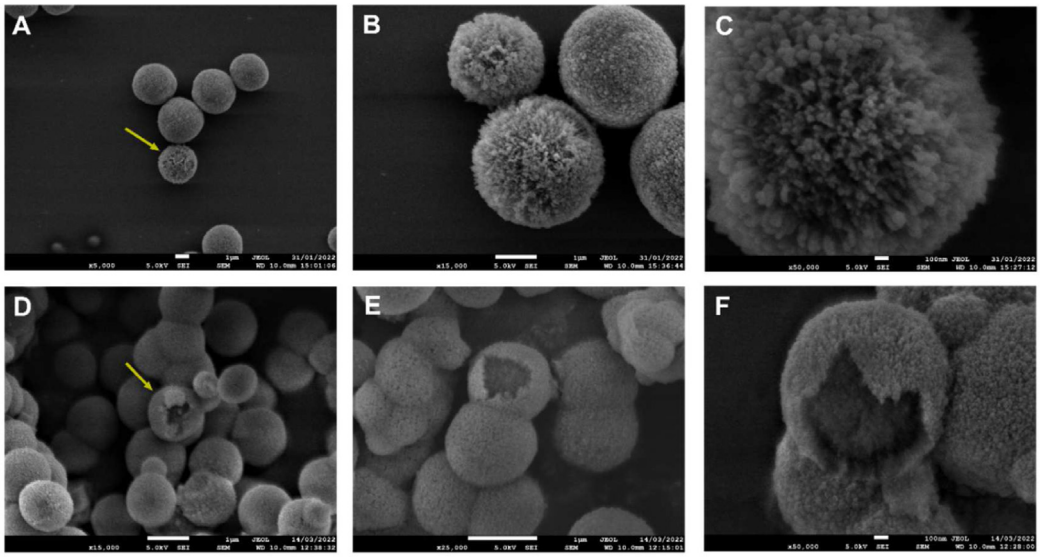

Fig. 11. SEM images of $CaCO_3$/AgNPs (A–C) and $CaCO_3$-PSS/AgNPs (D–F) after 2 h in MHB at 37°C. The yellow arrows in images A and D point to the hybrids with partially dissolved surfaces (higher magnification images allow to see this in more detail). Scale bar is 1 μm for image (A), (B), (D) and (E), and 100 nm.

development of a 'soft' corona composed of biomolecules that exist in high abundance, which then evolves to a 'hard' corona composed of biomolecules with high affinity to the surface [9,68,69]. The formation of the 'soft' corona is believed to occur within seconds to minutes, and the 'hard' corona, within hours [69]. This might explain the higher contents of AgNPs released in the first hour and then the slow release over the next 96 h.

The results presented here demonstrate that the proteins and carbohydrates in MHB changed the hybrids surface properties, as well as the interactions between $CaCO_3$ and AgNPs, resulting in a slow release over time. Although these results cannot be extrapolated to situations where the cargo and/or the medium are different, as the corona might potentiate or decrease the interactions between $CaCO_3$ and the cargo, it shows that vaterite is highly sensitive to the surrounding environment and that the release is not only controlled by recrystallization and dissolution at low pH, but also by the medium composition which can promote or halt the cargo release. Fig. 12 outlines the release route of AgNPs from vaterite in the presence of biomolecules.

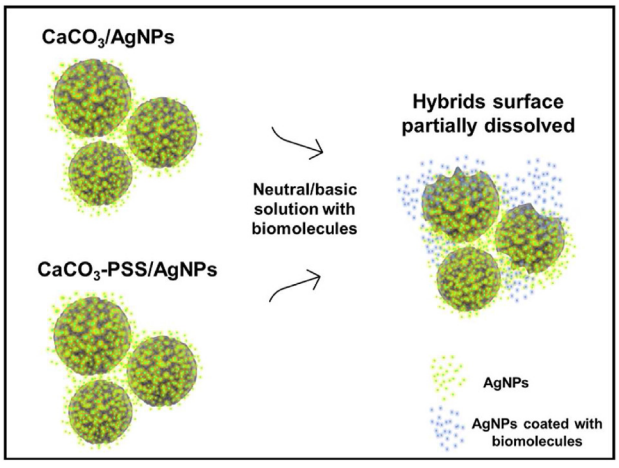

Fig. 12. Scheme of AgNPs release mechanism at neutral to basic pH in the presence of biomolecules.

3.5. Antibacterial activity

The alarming levels of antimicrobial resistance and decreasing number of drugs capable of eradicating the evolved microorganisms have raised awareness to control the release of antimicrobial agents and improve their delivery for better effectiveness and therapeutical outcomes. Herein, $CaCO_3$/AgNPs hybrids were developed to store, protect, carry and release AgNPs more efficiently.

Preliminary results presented in a recent work published by our group has demonstrated the antibacterial activity of $CaCO_3$/AgNPs hybrids [32]. Nonetheless, more studies are required to find out whether the activity of the AgNPs loaded into $CaCO_3$ was affected by the loading process. To that end antibacterial tests were carried out against E. *coli*, MRSA and *P. aeruginosa*, three bacterial isolates responsible for a high number of infections in hospital settings. $CaCO_3$/AgNPs hybrids were chosen instead of $CaCO_3$-PSS/AgNPs hybrids, as the last ones present a lower release of AgNPs in MHB at pH 7.4.

Before assessing the antibacterial activity of the hybrids, the content of AgNPs released from the $CaCO_3$/AgNPs hybrids in MHB was determined. As presented in Fig. S12, the amount of silver released ranged between 9.1 and 109.4 μg/ml, corresponding to 99.4% and 18.6% of the total amount of silver loaded into the hybrids at the concentrations ranging between 0.33 and 21 mg/ml, respectively. Similarly to the release studies in MHB, no recrystallization of the hybrids was detected after 24 h, as shown in the transmittance images. It was also verified that the amount of silver released increased with the concentration of hybrids, and then a plateau was reached when the hybrids concentration was between 10 and 21 mg/ml.

AgNPs are mainly found on the surface or close to the surface of $CaCO_3$ (Fig. S13), therefore when the concentration of $CaCO_3$/AgNPs increases, more hybrids are in suspension, which increases the surface area and release of AgNPs through the partial dissolution of the surface (Fig. 11) instead of the entire or more profound areas of the hybrids which do not carry AgNPs. This exposes more nanoparticles to the proteins and carbohydrates present in MHB, which seem to form a corona on their surface, decreasing the affinity to $CaCO_3$. The reduced affinity, associated with the fact that the

nanoparticles become poorly entrapped on the partially dissolved surfaces, promotes the release of the AgNPs. When there is an excess of hybrids, and the dissolution of the crystals necessary to reach the equilibrium only affects the surfaces of the $CaCO_3$/AgNPs hybrids, a plateau is reached, and the amount of silver released does not change with increasing concentrations of hybrids.

Fig. 13 presents the minimum concentration of silver required to inhibit the growth of planktonic bacteria and biofilms (MIC and MBIC, respectively) and kill the bacteria (MBC). Unloaded AgNPs were used as a control for comparison with the AgNPs released from the hybrids. The MIC, MBC and MBIC as a function of the hybrids concentration can be found in Fig. S14. The results show that the AgNPs released from the $CaCO_3$/AgNPs hybrids inhibited the growth of *E. coli*, MRSA and *P. aeruginosa* at 34 ± 12, 38 ± 22 and 17 ± 10 μg/ml, respectively. The AgNPs were also effective in killing and inhibiting the growth of biofilms.

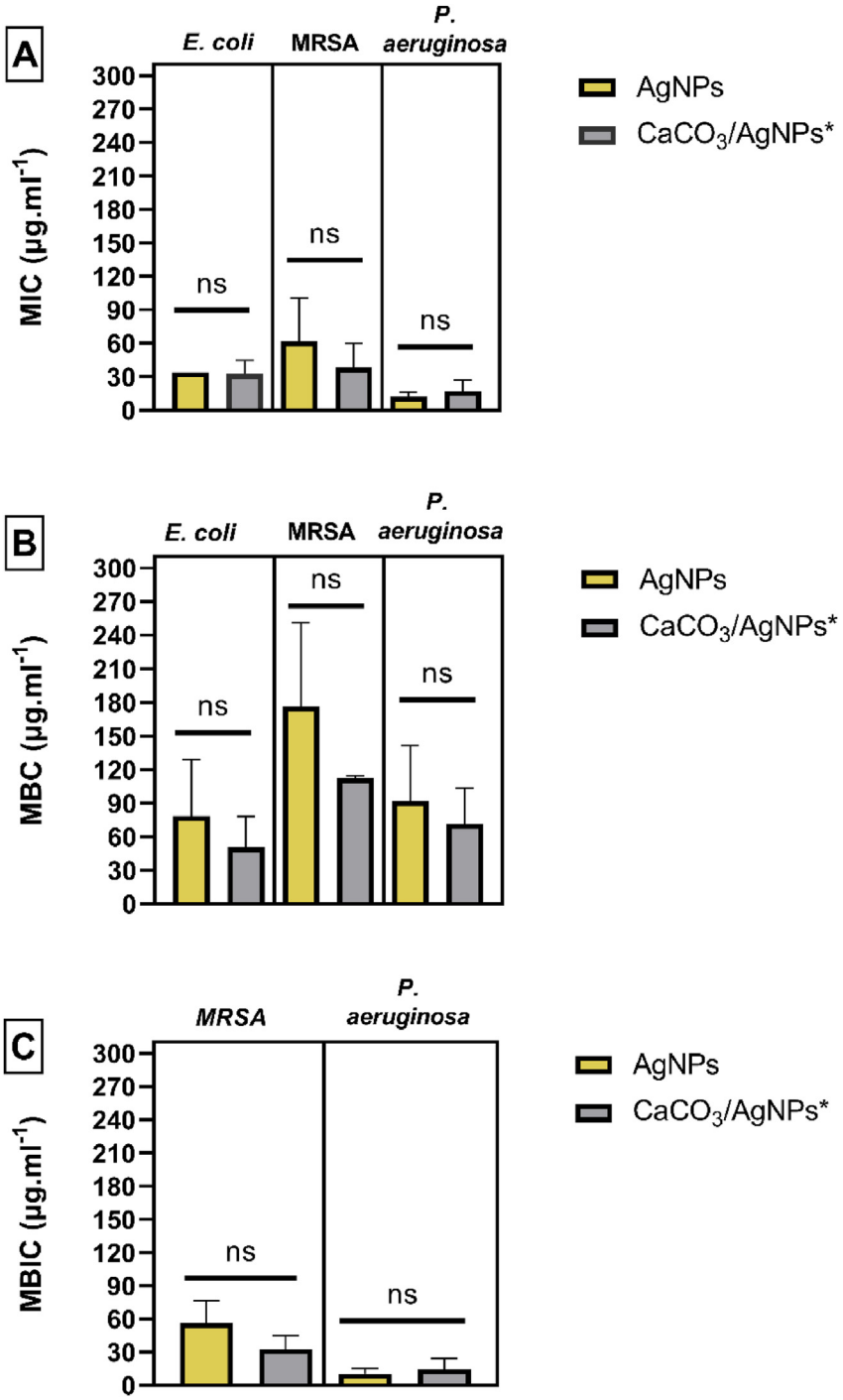

Fig. 13. MIC (A), MBC (B) and MBIC (C) (μg/ml) of AgNPs and $CaCO_3$/AgNPs against planktonic *E. coli*, MRSA and *P. aeruginosa*. Data corresponds to three to six repeats with three replicates each. Statistical analysis made using the *t*-test (normal distribution) and Mann-Whitney test (non-normal distribution). ns: not significant difference. $CaCO_3$/AgNPs*: concentration of silver released from $CaCO_3$/AgNPs hybrids determined on preliminary studies where the amount of silver released in MHB was quantified.

The bare $CaCO_3$ did not present bactericidal activity at concentrations equal to or below 21 mg/ml, which shows that the bactericidal activity of the hybrids was mostly promoted by the AgNPs.

Interestingly, as previously reported for the hybrids, the AgNPs presented better activity against *E. coli* and *P. aeruginosa* than against MRSA [32]. Despite the reason behind this effect not being fully understood and the lack of consensus, similar results have been reported elsewhere and is believed to result from structural differences between the membrane of gram-positive and gram-negative bacteria [70–72].

Importantly, in all the antibacterial tests performed, there were no significant differences between the antibacterial activity of the unloaded AgNPs and the AgNPs released from hybrids, which demonstrates that the loading steps and vaterite itself did not impair the activity of the AgNPs. The good antibacterial activity of the developed hybrids, allied with the controlled and targeted release, offers new opportunities to use and deliver active AgNPs more efficiently, and contribute to a more rational use of silver.

4. Conclusion

In this work, hybrids composed of vaterite $CaCO_3$ and AgNPs were produced for the protection and storage of AgNPs. To control the release of the cargo, Dex^{CM} and PSS were used to stabilise the hybrids by preventing the recrystallization of vaterite to calcite and consequent cargo release. Dex^{CM} partially prevented the recrystallization of the hybrids at contents equal to 4%, although it affected the uptake of AgNPs. On the other hand, 2% of PSS prevented the recrystallization without impairing the uptake of AgNPs.

The release of AgNPs from $CaCO_3$/AgNPs and $CaCO_3$-PSS/AgNPs hybrids was studied at different pH values, at closed and open-like conditions, and in the presence of high contents of biomolecules for a detailed elucidation of the release mechanisms. While the $CaCO_3$/AgNPs hybrids presented a recrystallisation-dependent release at higher pH values, the hybrids stabilized with PSS presented a targeted release at acid environments, with a burst release at pH 5 and no AgNPs being released at pH 7.4 and 9.0. New insights were also introduced about the effect of biomolecules on the release of AgNPs from the hybrids.

The antibacterial studies demonstrated that the hybrids developed protect the AgNPs without impairing their antibacterial properties against *E. coli*, MRSA and *P. aeruginosa*.

Overall, this work presents a simple approach to control the recrystallization of vaterite and consequent cargo (AgNPs) release. The detailed analysis of the release mechanism gives a complete insight into the challenges and viable solutions for the targeted and controlled release of active compounds from vaterite vectors, and highlights the impact of biomolecules in changing the affinity between the cargo and the vector, and consequently the release mechanism. While this work is focused on AgNPs, the findings can be extrapolated to other types of compounds loaded into $CaCO_3$, and will help future works on the design of vaterite vectors with features of controlled and targeted delivery.

CrediT authorship contribution statement

Ana M. Ferreira: Writing-Original Draft, Writing-Review & Editing, Conceptualization, Methodology, Validation, Formal analysis, Investigation. **AnnaVikulina:** Formal analysis, Writing- Review and Editing. **Gareth W. V. Cave:** Supervision, Writing-Review & Editing, Resources. **Michael Loughlin:** Supervision, Methodology, Writing-Review & Editing. **Valeria Puddu:** Supervision, Writing-Review & Editing. **DmitryVolodkin:** Supervision, Conceptualization, Validation, Writing-Review & Editing, Resources, Funding acquisition.

Funding

This work was supported by the Marie Skłodowska-Curie PhD Fellowship programme, EC Grant Agreement No: 801604-DTA3-H2020-MSCA-COFUND-2017, and QR fund from NTU 2022/23.

Declaration of competing interest

The authors declare that they have no known competing financial interests or personal relationships that could have appeared to influence the work reported in this paper.

Data availability

Data will be made available on request.

Acknowledgments

The authors thank Graham Hickman from the Nottingham Trent University for the assistance with TEM imaging.

Appendix A. Supplementary data

Supplementary data to this article can be found online at https://doi.org/10.1016/j.mtchem.2023.101586.

References

[1] A.M. Ferreira, A.S. Vikulina, D. Volodkin, CaCO3 crystals as versatile carriers for controlled delivery of antimicrobials, J. Contr. Release 328 (2020) 470–489, https://doi.org/10.1016/j.jconrel.2020.08.061.
[2] M. Ahonen, A. Kahru, A. Ivask, K. Kasemets, S. Kõljalg, P. Mantecca, I.V. Vrček, M.M. Keinänen-Toivola, F. Crijns, Proactive approach for safe use of antimicrobial coatings in healthcare settings: opinion of the COST action network AMiCI, Int. J. Environ. Res. Publ. Health 14 (2017) 1–23, https://doi.org/10.3390/IJERPH14040366.
[3] B. Nowack, H.F. Krug, M. Height, 120 years of nanosilver history: implications for policy makers, Environ. Sci. Technol. 45 (2011) 7593–7595, https://doi.org/10.1021/es2017895.
[4] Z. Ni, X. Gu, Y. He, Z. Wang, X. Zou, Y. Zhao, L. Sun, Synthesis of silver nanoparticle-decorated hydroxyapatite (HA@Ag) poriferous nanocomposites and the study of their antibacterial activities, RSC Adv. 8 (2018) 41722–41730, https://doi.org/10.1039/c8ra08148d.
[5] W. Shao, X. Liu, H. Min, G. Dong, Q. Feng, S. Zuo, Preparation, characterization, and antibacterial activity of silver nanoparticle-decorated graphene oxide nanocomposite, Appl. Mater. Interfaces 7 (2015) 6966–6973, https://doi.org/10.1021/acsami.5b00937.
[6] S. Borse, M. Temgire, A. Khan, S. Joshi, Photochemically assisted one–pot synthesis of PMMA embedded silver nanoparticles: antibacterial efficacy and water treatment, RSC Adv. 1 (2016) 1–8, https://doi.org/10.1039/b000000x.
[7] P. Ma, L. Jiang, M. Yu, W. Dong, M. Chen, Green antibacterial nanocomposites from poly(lactide)/poly(butylene adipate-co-terephthalate)/nanocrystal cellulose – silver nanohybrids, ACS Sustain. Chem. Eng. 4 (2016) 6417–6426, https://doi.org/10.1021/acssuschemeng.6b01106.
[8] S. Loher, O.D. Schneider, T. Maienfisch, S. Bokorny, W.J. Stark, Antimicrobial surfaces micro-organism-triggered release of silver nanoparticles from biodegradable oxide carriers allows preparation of self-sterilizing polymer surfaces, Small 4 (2008) 824–832, https://doi.org/10.1002/smll.200800047.
[9] P.C. Ke, S. Lin, W.J. Parak, T.P. Davis, F. Caruso, A decade of the protein corona, ACS Nano 11 (2017) 11773–11776, https://doi.org/10.1021/acsnano.7b08008.
[10] R. Beck, J.P. Andreassen, The onset of spherulitic growth in crystallization of calcium carbonate, J. Cryst. Growth 312 (2010) 2226–2238, https://doi.org/10.1016/j.jcrysgro.2010.04.037.
[11] M. Maleki Dizaj, M. Barzegar-Jalali, Zarrintan, K. Adibkia, F. Lotfipour, Calcium carbonate nanoparticles as cancer drug delivery system, Expert Opin. Drug Deliv. 12 (2015) 1649–1660, https://doi.org/10.1517/17425247.2015.1049530.
[12] X. He, T. Liu, Y. Chen, D. Cheng, X. Li, Y. Xiao, Y. Feng, Calcium carbonate nanoparticle delivering vascular endothelial growth factor-C siRNA effectively inhibits lymphangiogenesis and growth of gastric cancer in vivo, Cancer Gene Ther. 15 (2008) 193–202, https://doi.org/10.1038/sj.cgt.7701122.
[13] S. Chen, F. Li, R. Zhuo, S. Cheng, Molecular biosystems efficient non-viral gene delivery mediated by nanostructured calcium carbonate in solution-based transfection and solid-phase transfection, Mol. Biosyst. 7 (2011) 2841–2847, https://doi.org/10.1039/c1mb05147d.

[14] A.S. Vikulina, N.A. Feoktistova, N.G. Balabushevich, A.G. Skirtach, D. Volodkin, The mechanism of catalase loading into porous vaterite CaCO3 crystals by co-synthesis, Phys. Chem. Chem. Phys. 20 (2018) 8822–8831, https://doi.org/10.1039/c7cp07836f.
[15] O. Lishchynskyi, Y. Stetsyshyn, J. Raczkowska, K. Awsiuk, B. Orzechowska, A. Abalymov, A.G. Skirtach, A. Bernasik, S. Nastyshyn, A. Budkowski, Fabrication and impact of fouling-reducing temperature-responsive POEGMA coatings with embedded CaCO3 nanoparticles on different cell lines, Mater 14 (2021) 1417, https://doi.org/10.3390/MA14061417.
[16] C. Matei, D. Berger, A. Dumbrava, M.D. Radu, E. Gheorghe, Calcium carbonate as silver carrier in composite materials obtained in green seaweed extract with topical applications, J. Sol. Gel Sci. Technol. 93 (2020) 315–323, https://doi.org/10.1007/s10971-019-05145-6.
[17] M. Długosz, M. Bulwan, G. Kania, M. Nowakowska, S. Zapotoczny, Hybrid calcium carbonate/polymer microparticles containing silver nanoparticles as antibacterial agents, J. Nanopart. Res. 14 (2012) 1–8, https://doi.org/10.1007/s11051-012-1313-7.
[18] H. Zhang, K. Wang, G. Fan, J. Lin, L. Huang, R. Xiang, al -, B. Le Thi, R. Shi, B. Duc Long, O. Długosz, K. Lis, M. Banach, Synthesis and antimicrobial properties of CaCO3-nAg and nAg-CaCO3 nanocomposites, Nanotechnology 32 (2020) 1–11, https://doi.org/10.1088/1361-6528/ABBCAA.
[19] M. Ueda, T. Yokota, M. Honda, P.N. Lim, N. Osaka, M. Makita, Y. Nishikawa, T. Kasuga, M. Aizawa, Regulating size of silver nanoparticles on calcium carbonate via ultrasonic spray for effective antibacterial efficacy and sustained release, Mater. Sci. Eng. C 125 (2021), 112083, https://doi.org/10.1016/j.msec.2021.112083.
[20] E. Bolli, S. Kaciulis, A. Mezzi, V. Ambrogi, M. Nocchetti, L. Latterini, A. Di Michele, G. Padeletti, Hydroxyapatite functionalized calcium carbonate composites with Ag nanoparticles: an integrated characterization study, Nanomater 11 (2021) 2263, https://doi.org/10.3390/nano11092263.
[21] V. Ambrogi, G. Quaglia, D. Pietrella, M. Nocchetti, A. Di Michele, E. Bolli, S. Kaciulis, A. Mezzi, G. Padeletti, L. Latterini, Silver@Hydroxyapatite functionalized calcium carbonate composites: characterization, antibacterial and antibiofilm activities and cytotoxicity, Appl. Surf. Sci. 586 (2022) 1–11, https://doi.org/10.1016/j.apsusc.2022.152760.
[22] U.A. Hasanova, A.R. Aliyev, I.R. Hasanova, E.M. Gasimov, S.F. Hajiyeva, A.A. Israyilova, K.G. Ganbarov, Z.O. Gakhramanova, P.F. Huseynova, N.R. Amrahov, Functionalization of surgical meshes with antibacterial hybrid Ag@crown nanoparticles, Dig. J. Nanomater. Biostruct. 17 (2022) 11–19, https://doi.org/10.15251/DJNB.2022.171.11.
[23] K.H. Min, E.Y. Jang, H.J. Lee, Y.S. Hwang, J.I. Ryu, J.H. Moon, S.C. Lee, pH-Responsive mineralized nanoparticles for bacteria-triggered topical release of antibiotics, J. Ind. Eng. Chem. 71 (2019) 210–219, https://doi.org/10.1016/j.jiec.2018.11.027.
[24] G. Begum, T.N. Reddy, K.P. Kumar, K. Dhevendar, S. Singh, M. Amarnath, S. Misra, V.K. Rangari, R.K. Rana, In situ strategy to encapsulate antibiotics in a bioinspired CaCO3 structure enabling pH-sensitive drug release apt for therapeutic and imaging applications, ACS Appl. Mater. Interfaces 8 (2016) 22056–22063, https://doi.org/10.1021/acsami.6b07177.
[25] N.G. Balabushevich, E.A. Kovalenko, I.M. Le-Deygen, L.Y. Filatova, D. Volodkin, A.S. Vikulina, Hybrid CaCO3-mucin crystals: effective approach for loading and controlled release of cationic drugs, Mater. Des. 182 (2019) 1–12, https://doi.org/10.1016/j.matdes.2019.108020.
[26] P. Bots, L.G. Benning, J.D. Rodriguez-Blanco, T. Roncal-Herrero, S. Shaw, Mechanistic insights into the crystallization of amorphous calcium carbonate (ACC), Cryst, Growth Des. 12 (2012) 3806–3814, https://doi.org/10.1021/cg300676b.
[27] M.A. Hood, K. Landfester, R. Muñoz-Espí, The role of residue acidity on the stabilization of vaterite by amino acids and oligopeptides, Cryst. Growth Des. 14 (2014) 1077–1085, https://doi.org/10.1021/cg401580y.
[28] A. Sergeeva, R. Sergeev, E. Lengert, A. Zakharevich, B. Parakhonskiy, D. Gorin, S. Sergeev, D. Volodkin, Composite magnetite and protein containing CaCO3 crystals. External manipulation and vaterite → calcite recrystallization-mediated release performance, ACS Appl. Mater. Interfaces 7 (2015) 21315–21325, https://doi.org/10.1021/acsami.5b05848.
[29] B.V. Parakhonskiy, C. Foss, E. Carletti, M. Fedel, A. Haase, A. Motta, C. Migliaresi, R. Antolini, Tailored intracellular delivery via a crystal phase transition in 400 nm vaterite particles, Biomater. Sci. 1 (2013) 1273–1281, https://doi.org/10.1039/c3bm60141b.
[30] G. Choukrani, B. Maharjan, C.H. Park, C.S. Kim, A.R. Kurup Sasikala, Biocompatible superparamagnetic sub-micron vaterite particles for thermo-chemotherapy: from controlled design to in vitro anticancer synergism, Mater. Sci. Eng. C. 106 (2020) 1–12, https://doi.org/10.1016/j.msec.2019.110226.
[31] B.V. Parakhonskiy, A. Haase, R. Antolini, Sub-micrometer vaterite containers: synthesis, substance loading, and release, Angew. Chem. Int. Ed. 51 (2012) 1195–1197, https://doi.org/10.1002/anie.201104316.
[32] A.M. Ferreira, A. Vikulina, G.W.V. Cave, M. Loughlin, V. Puddu, D. Volodkin, Vaterite vectors for the protection, storage and release of silver nanoparticles, J. Colloid Interface Sci. 631 (2023) 165–180, https://doi.org/10.1016/J.JCIS.2022.10.094.
[33] E. Izak-Nau, A. Huk, B. Reidy, H. Uggerud, M. Vadset, S. Eiden, M. Voetz, M. Himly, A. Duschl, M. Dusinska, I. Lynch, Impact of storage conditions and storage time on silver nanoparticles' physicochemical properties and implications for their biological effects, RSC Adv. 5 (2015) 84172–84185, https://doi.org/10.1039/c5ra10187e.
[34] D.V. Volodkin, A.I. Petrov, M. Prevot, G.B. Sukhorukov, Matrix polyelectrolyte microcapsules: new system for macromolecule encapsulation, Langmuir 20 (2004) 3398–3406, https://doi.org/10.1021/la036177z.
[35] I. Khan, K. Saeed, I. Khan, Nanoparticles: properties, applications and toxicities, Arab. J. Chem. 12 (2019) 908–931, https://doi.org/10.1016/j.arabjc.2017.05.011.
[36] D. Paramelle, A. Sadovoy, S. Gorelik, P. Free, J. Hobley, D.G. Fernig, A rapid method to estimate the concentration of citrate capped silver nanoparticles from UV-visible light spectra, Analyst 139 (2014) 4855–4861, https://doi.org/10.1039/c4an00978a.
[37] C.G. Kontoyannis, N.V. Vagenas, Calcium carbonate phase analysis using XRD and FT-Raman spectroscopy, Analyst 125 (2000) 251–255, https://doi.org/10.1039/a908609i.
[38] Mathematical models of drug release, in: M.L. Bruschi (Ed.), Strategy to Modify Drug Release from Pharm. Syst., Woodhead Publishing, 2015, pp. 63–86, https://doi.org/10.1016/b978-0-08-100092-2.00005-9.
[39] P. Costa, J.M. Sousa Lobo, Modeling and comparison of dissolution profiles, Eur. J. Pharm. Sci. 13 (2001) 123–133, https://doi.org/10.1016/S0928-0987(01)00095-1.
[40] I. Wiegand, K. Hilpert, R.E.W. Hancock, Agar and broth dilution methods to determine the minimal inhibitory concentration (MIC) of antimicrobial substances, Nat. Protoc. 3 (2008) 163–175, https://doi.org/10.1038/nprot.2007.521.
[41] A. Ivanova, K. Ivanova, A. Tied, T. Heinze, T. Tzanov, Layer-by-layer coating of aminocellulose and quorum quenching acylase on silver nanoparticles synergistically eradicate bacteria and their biofilms, Adv. Funct. Mater. 30 (2020) 1–9, https://doi.org/10.1002/adfm.202001284.
[42] S. Sareen, V. Mutreja, S. Singh, B. Pal, Highly dispersed Au, Ag and Cu nanoparticles in mesoporous SBA-15 for highly selective catalytic reduction of nitroaromatics, RSC Adv. 5 (2015) 184–190, https://doi.org/10.1039/c4ra10050f.
[43] K. Lemański, M. Michalska, M. Ptak, M. Małecka, A. Szysiak, Surface modification using silver nanoparticles for Y4Al2O9:Nd – synthesis and their selected studies, J. Mol. Struct. 1202 (2020) 1–6, https://doi.org/10.1016/j.molstruc.2019.127363.
[44] B.V. Parakhonskiy, A.M. Yashchenok, S. Donatan, D.V. Volodkin, F. Tessarolo, R. Antolini, H. Möhwald, A.G. Skirtach, Macromolecule loading into spherical, elliptical, star-like and cubic calcium carbonate carriers, ChemPhysChem 15 (2014) 2817–2822, https://doi.org/10.1002/cphc.201402136.
[45] A. Vikulina, J. Webster, D. Voronin, E. Ivanov, R. Fakhrullin, V. Vinokurov, D. Volodkin, Mesoporous additive-free vaterite CaCO3 crystals of untypical sizes: from submicron to giant, Mater. Des. 197 (2021) 1–9, https://doi.org/10.1016/j.matdes.2020.109220.
[46] D.B. Trushina, T.N. Borodina, S. Belyakov, M.N. Antipina, Calcium carbonate vaterite particles for drug delivery: advances and challenges, Mater. Today Adv. 14 (2022) 1–17, https://doi.org/10.1016/j.mtadv.2022.100214.
[47] X. Wang, R. Kong, X. Pan, H. Xu, D. Xia, H. Shan, J.R. Lu, Role of ovalbumin in the stabilization of metastable vaterite in calcium carbonate biomineralization, J. Phys. Chem. B 113 (2009) 8975–8982, https://doi.org/10.1021/jp810281f.
[48] S.S. Wang, A. Picker, H. Cölfen, A.W. Xu, Heterostructured calcium carbonate microspheres with calcite equatorial loops and vaterite spherical cores, Angew. Chem. Int. Ed. 52 (2013) 6317–6321, https://doi.org/10.1002/anie.201301184.
[49] M. Yang, X. Jin, Q. Huang, Facile synthesis of vaterite core-shell microspheres, Colloids Surf. A Physicochem. Eng. Asp. 374 (2011) 102–107, https://doi.org/10.1016/J.COLSURFA.2010.11.018.
[50] E.F. Souza, J.A.R. Ambrósio, B.C.S. Pinto, M. Beltrame, K.K. Sakane, J.G. Pinto, J. Ferreira-Strixino, E.P. Gonçalves, A.R. Simioni, Vaterite submicron particles designed for photodynamic therapy in cells, Photodiagn. Photodyn. Ther. 31 (2020) 1–7, https://doi.org/10.1016/J.PDPDT.2020.101913.
[51] Y. Wang, Y.X. Moo, C. Chen, P. Gunawan, R. Xu, Fast precipitation of uniform CaCO3 nanospheres and their transformation to hollow hydroxyapatite nanospheres, J. Colloid Interface Sci. 352 (2010) 393–400, https://doi.org/10.1016/J.JCIS.2010.08.060.
[52] J. Campbell, A.M. Ferreira, L. Bowker, J. Hunt, D. Volodkin, A. Vikulina, Dextran and its derivatives: biopolymer additives for the modulation of vaterite CaCO3 crystal morphology and adhesion to cells, Adv. Mater. Interf. 9 (2022) 1–10, https://doi.org/10.1002/admi.202201196.
[53] P.J.M. Smeets, K.R. Cho, R.G.E. Kempen, N.A.J.M. Sommerdijk, J.J. De Yoreo, Calcium carbonate nucleation driven by ion binding in a biomimetic matrix revealed by in situ electron microscopy, Nat. Mater. 14 (2015) 394–399, https://doi.org/10.1038/nmat4193.
[54] Z. Zhang, B. Yang, H. Tang, X. Chen, B. Wang, High-yield synthesis of vaterite CaCO3 microspheres in ethanol/water: structural characterization and formation mechanisms, J. Mater. Sci. 50 (2015) 5540–5548, https://doi.org/10.1007/s10853-015-9101-2.
[55] M. Sato, S. Matsuda, Structure of vaterite and infrared spectra, Zeitsch. Fur Krist. New Cryst. Struct. 129 (1969) 405–410, https://doi.org/10.1524/zkri.1969.129.5-6.405.
[56] F.A. Andersen, L. Brečević, Infrared spectra of amorphous and crystalline calcium carbonate, Acta Chem. Scand. 45 (1991) 1018–1024, https://doi.org/10.3891/acta.chem.scand.45-1018.

[57] L. Pérez-Villarejo, F. Takabait, L. Mahtout, B. Carrasco-Hurtado, D. Eliche-Quesada, P.J. Sánchez-Soto, Synthesis of vaterite CaCO3 as submicron and nanosized particles using inorganic precursors and sucrose in aqueous medium, Ceram. Int. 44 (2018) 5291–5296, https://doi.org/10.1016/j.ceramint.2017.12.142.
[58] P. Sow, IR – Spectroscopic Investigations of the Kinetics of Calcium Carbonate Precipitation, University of Konstanz, 2016. https://d-nb.info/120201299X/34.
[59] L. Addadi, S. Raz, S. Weiner, Taking advantage of disorder: amorphous calcium carbonate and its roles in biomineralization, Adv. Mater. 15 (2003) 959–970, https://doi.org/10.1002/adma.200300381.
[60] J.C. Yang, M.J. Jablonsky, J.W. Mays, NMR and FT-IR studies of sulfonated styrene-based homopolymers and copolymers, Polymer (Guildf) 43 (2002) 5125–5132, https://doi.org/10.1016/S0032-3861(02)00390-7.
[61] Y.B. Song, S.N. Lv, C.J. Cheng, G.L. Ni, X.W. Xie, W. Huang, Z.G. Zhao, Fast and highly-efficient removal of methylene blue from aqueous solution by poly(-styrenesulfonic acid-co-maleic acid)-sodium-modified magnetic colloidal nanocrystal clusters, Appl. Surf. Sci. 324 (2015) 854–863, https://doi.org/10.1016/j.apsusc.2014.11.060.
[62] M. Braglia, I.V. Ferrari, T. Djenizian, S. Kaciulis, P. Soltani, M.L. Di Vona, P. Knauth, Bottom-up electrochemical deposition of poly(styrene sulfonate) on nanoarchitectured electrodes, ACS Appl. Mater. Interf. 9 (2017) 22902–22910, https://doi.org/10.1021/ACSAMI.7B04335/ASSET/IMAGES/ACSAMI.7B04335.SOCIAL.JPEG_V03.
[63] Y. Li, S. Zhou, H. Song, T. Yu, X. Zheng, Q. Chu, CaCO3 nanoparticles incorporated with KAE to enable amplified calcium overload cancer therapy, Biomaterials 277 (2021) 1–10, https://doi.org/10.1016/j.biomaterials.2021.121080.
[64] O. Gusliakova, R. Verkhovskii, A. Abalymov, E. Lengert, A. Kozlova, V. Atkin, O. Nechaeva, A. Morrison, V. Tuchin, Y. Svenskaya, Transdermal platform for the delivery of the antifungal drug naftifine hydrochloride based on porous vaterite particles, Mater. Sci. Eng. C 119 (2021) 1–11, https://doi.org/10.1016/j.msec.2020.111428.
[65] Y.I. Svenskaya, A.M. Pavlov, D.A. Gorin, D.J. Gould, B.V. Parakhonskiy, G.B. Sukhorukov, Photodynamic therapy platform based on localized delivery of photosensitizer by vaterite submicron particles, Colloids Surf. B Biointerf. 146 (2016) 171–179, https://doi.org/10.1016/j.colsurfb.2016.05.090.
[66] D.B. Trushina, T.N. Borodina, V.V. Artemov, T.V. Bukreeva, Immobilization of photoditazine on vaterite porous particles and analysis of the system stability in model media, Tech. Phys. 63 (2018) 1345–1351, https://doi.org/10.1134/S1063784218090220.
[67] O. Gusliakova, E.N. Atochina-Vasserman, O. Sindeeva, S. Sindeev, S. Pinyaev, N. Pyataev, V. Revin, G.B. Sukhorukov, D. Gorin, A.J. Gow, Use of submicron vaterite particles serves as an effective delivery vehicle to the respiratory portion of the lung, Front. Pharmacol. 9 (2018) 1–13, https://doi.org/10.3389/fphar.2018.00559.
[68] A. Lesniak, F. Fenaroli, M.P. Monopoli, C. Åberg, K.A. Dawson, A. Salvati, Effects of the presence or absence of a protein corona on silica nanoparticle uptake and impact on cells, ACS Nano 6 (2012) 5845–5857, https://doi.org/10.1021/nn300223w.
[69] J.S. Gebauer, M. Malissek, S. Simon, S.K. Knauer, M. Maskos, R.H. Stauber, W. Peukert, L. Treuel, Impact of the nanoparticle–protein corona on colloidal stability and protein structure, Langmuir 28 (2012) 9673–9678, https://doi.org/10.1021/la301104a.
[70] J.S. Kim, E. Kuk, K.N. Yu, J.H. Kim, S.J. Park, H.J. Lee, S.H. Kim, Y.K. Park, Y.H. Park, C.Y. Hwang, Y.K. Kim, Y.S. Lee, D.H. Jeong, M.H. Cho, Antimicrobial effects of silver nanoparticles, Nanomed. Nanotechnol. Biol. Med. 3 (2007) 95–101, https://doi.org/10.1016/j.nano.2006.12.001.
[71] J. Lopez-Esparza, L. Francisco Espinosa-Cristobal, A. Donohue-Cornejo, S.Y. Reyes-Lopez, Antimicrobial activity of silver nanoparticles in polycaprolactone nanofibers against gram-positive and gram-negative bacteria, Ind. Eng. Chem. Res. 55 (2016) 12532–12538, https://doi.org/10.1021/acs.iecr.6b02300.
[72] C.H. Chen, S.H. Chen, K.T. Shalumon, J.P. Chen, Dual functional core-sheath electrospun hyaluronic acid/polycaprolactone nanofibrous membranes embedded with silver nanoparticles for prevention of peritendinous adhesion, Acta Biomater. 26 (2015) 225–235, https://doi.org/10.1016/j.actbio.2015.07.041.